

# Characterizing the Youngest Herschel-detected Protostars I. Envelope Structure Revealed by CARMA Dust Continuum Observations

John J. Tobin<sup>1,8,9</sup>, Amelia M. Stutz<sup>2</sup>, S. Thomas Megeath<sup>3</sup>, William J. Fischer<sup>3</sup>, Thomas Henning<sup>2</sup>, Sarah E. Ragan<sup>2</sup>, Babar Ali<sup>4</sup>, Thomas Stanke<sup>5</sup>, P. Manoj<sup>6</sup>, Nuria Calvet<sup>7</sup>, Lee Hartmann<sup>7</sup>

## ABSTRACT

We present CARMA 2.9 mm dust continuum emission observations of a sample of 14 Herschel-detected Class 0 protostars in the Orion A and B molecular clouds, drawn from the PACS Bright Red Sources (PBRs) sample (Stutz et al.). These objects are characterized by very red 24  $\mu\text{m}$  to 70  $\mu\text{m}$  colors and prominent submillimeter emission, suggesting that they are very young Class 0 protostars embedded in dense envelopes. We detect all of the PBRs in 2.9 mm continuum emission and emission from 4 protostars and 1 starless core in the fields toward the PBRs; we also report 1 new PBRs source. The ratio of 2.9 mm luminosity to bolometric luminosity is higher by a factor of  $\sim 5$  on average, compared to other well-studied protostars in the Perseus and Ophiuchus clouds. The 2.9 mm visibility amplitudes for 6 of the 14 PBRs are very flat as a function of uv-distance, with more than 50% of the source emission arising from radii  $< 1500$  AU. These

---

<sup>1</sup>National Radio Astronomy Observatory, Charlottesville, VA 22903

<sup>2</sup>Max-Planck-Institut für Astronomie, D-69117 Heidelberg, Germany

<sup>3</sup>Ritter Astrophysical Observatory, Department of Physics and Astronomy, University of Toledo, Toledo, OH 43560

<sup>4</sup>NASA *Herschel* Science Center, California Institute of Technology, Pasadena, CA 91125, USA

<sup>5</sup>European Southern Observatory, 85748 Garching bei München, Germany

<sup>6</sup>Department of Astronomy and Astrophysics, Tata Institute of Fundamental Research, Colaba, Mumbai 400005, India

<sup>7</sup>Department of Astronomy, University of Michigan, Ann Arbor, MI 48109

<sup>8</sup>Hubble Fellow

<sup>9</sup>Current Address: Leiden Observatory, Leiden University, P.O. Box 9513, 2300-RA Leiden, The Netherlands; tobin@strw.leidenuniv.nl

flat visibility amplitudes are most consistent with spherically symmetric envelope density profiles with  $\rho \propto R^{-2.5}$ . Alternatively, there could be a massive unresolved structure like a disk or a high-density inner envelope departing from a smooth power-law. The large amount of mass on scales  $< 1500$  AU (implying high average central densities) leads us to suggest that the PBRS with flat visibility amplitude profiles are the youngest PBRS and may be undergoing a brief phase of high mass infall/accretion and are possibly among the youngest Class 0 protostars. The PBRS with more rapidly declining visibility amplitudes still have large envelope masses, but could be slightly more evolved.

## 1. Introduction

Stars form as a result of the gravitational collapse of clouds of gas and dust. This process can take place in isolated Bok globules (e.g., B335; Keene et al. 1983; Stutz et al. 2008, 2010) or within fragmented giant molecular clouds (e.g. Orion; Johnstone & Bally 1999; Motte & André 2001; Polychroni et al. 2013). The earliest recognizable phase of the star formation process is the Class 0 phase (André et al. 1993), the beginning of which is marked by the formation of a hydrostatically supported protostar within an infalling cloud of gas and dust. The robust identification of the youngest sources is imperative for characterizing the initial conditions at the time of protostar formation, before feedback from the formation process significantly alters local physical conditions (e.g., Arce & Sargent 2006; Offner & Arce 2014) and probe the earliest stages of the collapse of the gas onto nascent protostars (e.g., Foster & Chevalier 1993). The density profile, overall mass, and angular momentum of the initially collapsing envelope will determine the potential for fragmentation, how quickly the protostar may accumulate mass, and the growth of the circumstellar disk.

At the start of protostellar collapse, just prior to protostar formation, there is a theoretical prediction of a short-lived ( $\sim 1000$  yr) first hydrostatic core (FHSC), a phase just before or at the start of the Class 0 phase (e.g., Larson 1969; Commerçon et al. 2012). Several candidate FHSCs have been identified (Enoch et al. 2010; Chen et al. 2010; Pineda et al. 2011; Schnee et al. 2012), but their identification as true FHSCs remains uncertain, given that these objects could simply be very low luminosity protostars (e.g., VeLLOs; Bourke et al. 2006). Since the FHSC phase is thought to be short, it is unlikely that many of the candidates in the nearest star forming regions (i.e. Perseus, Taurus, Ophiuchus) are true FHSCs due to their relatively small populations of protostars. Above all else, it is uncertain if there is truly a FHSC phase and if it can be uniquely distinguished from Class 0 protostars. Nonetheless, detecting and characterizing the youngest protostellar sources are key steps

towards understanding the star formation process. To capture short-lived phenomena, like the early Class 0 protostars and FHSCs, it is advantageous to look toward more populous regions of star formation.

The Orion molecular clouds are the nearest regions of active star formation. The *Spitzer* Orion survey by Megeath et al. (2012) found 488 protostellar candidates amongst a total of  $\sim 3000$  young stellar objects. A subset of 329 protostars from this sample were selected for observations in the far-infrared as part of the *Herschel* Orion Protostar Survey (HOPS) (e.g., Fischer et al. 2010; Stanke et al. 2010; Ali et al. 2010; Manoj et al. 2013). Within the fields observed by HOPS, Stutz et al. (2013), hereafter ST13, serendipitously identified 11 protostars with bright  $70\ \mu\text{m}$  and  $160\ \mu\text{m}$  emission that were not part of the original *Spitzer*-selected sample. At  $24\ \mu\text{m}$ , these sources were either non-detections (8 sources) or so faint that they were flagged as potential extragalactic contamination in the *Spitzer* surveys (Megeath et al. 2012; Kryukova et al. 2012). Moreover, within the original HOPS sample, 7 protostars had  $[24\ \mu\text{m}] - [70\ \mu\text{m}]$  colors (in  $\log(\lambda F_\lambda)$  space) redder than 1.65, consistent with the *Herschel*-detected sources. ST13 refers to the 18 protostars satisfying the extremely red color criterion as the PACS Bright Red Sources (PBRs).

Analysis of the PBRs spectral energy distributions (SEDs) by ST13, which were augmented by APEX  $350\ \mu\text{m}$  and  $870\ \mu\text{m}$  mapping, found that these PBRs sources have very cold bolometric temperatures ( $T_{\text{bol}}$ ; Myers & Ladd 1993) (29 K to 45 K) and high ratios of submillimeter luminosity to bolometric luminosity ( $L_{\text{bol}}$ ) (0.6% to 6.1%). Most PBRs are not detected shortward of  $24\ \mu\text{m}$ , but some display faint features in the *Spitzer* IRAC  $4.5\ \mu\text{m}$  band, possibly indicative of shocked  $\text{H}_2$  emission associated with outflows. Despite their deeply embedded nature, sources emitting at  $70\ \mu\text{m}$  must be self-luminous. For example, starless core models show that the emission would otherwise be too faint to detect at  $70\ \mu\text{m}$  (Ragan et al. 2012, ST13). It is important to point out that the PBRs sources are *not* low-luminosity objects like the VeLLOs (e.g., Bourke et al. 2006) since they have  $L_{\text{bol}}$  ranging between  $0.65\ L_\odot$  and  $30.6\ L_\odot$ , with the median being  $\sim 3\ L_\odot$ . These luminosities are large enough such that they are not dominated by external heating (Dunham et al. 2008).

The characteristics of the PBRs indicate that these protostars could be very young Class 0 sources with very dense envelopes (ST13). There is, however, a degeneracy in the interpretation of protostar SEDs between envelope density and inclination due to bipolar cavities being evacuated by the outflows. The envelope properties were also difficult to study with only the APEX submillimeter (submm) data available in ST13, due to the low resolution and blending of the envelope emission with extended cloud structure. Furthermore, the lack emission shortward of  $10\ \mu\text{m}$  toward most PBRs, made the inclinations impossible to constrain from SED modeling. The only way to derive more detailed envelope properties,

independent of inclination, is to observe these sources with an interferometer.

We have obtained observations of a subset of the PBRs sample with the Combined Array for Research in Millimeter-wave Astronomy (CARMA). There are a total of 19 PBRs, 18 of which were presented in ST13 and 1 additional PBRs will be described in this paper. We have observed 14 PBRs, focusing on the new, *Herschel*-detected subset of PBRs. We focused on this subset because they had the least amount of complementary data and non-detections at most wavelengths shorter than  $70\ \mu\text{m}$ . We observed the PBRs in both the dust continuum and spectral line emission to examine both the envelope and outflow properties of these sources; the outflow results will be presented in a future paper. We discuss the observations in Section 2, our results for the dust continuum emission and model comparison are given in Section 3, we discuss the results within the broader context of star formation in Section 4, and summarize our main conclusions in Section 5.

## 2. CARMA Observations and Data Reduction

CARMA is a heterogeneous interferometer array comprised of 23 antennas (6 - 10.4 m, 9 - 6.1 m, and 8 - 3.5 m) located in the Inyo mountains of California. Our observations were carried out with the main, 15-element CARMA array using the 10.4 m and 6.1 m antennas in two configurations. We observed a subset of the PBRs identified in ST13 with CARMA in the D configuration during late 2012 and early 2014. We also followed-up a subset of the sources observed in D-configuration with higher-resolution observations in C-configuration in early 2014. The angular resolutions in D and C configurations were  $\sim 5''$  and  $\sim 2''$  respectively. The central frequency was 107.77 GHz and four spectral windows were configured for 500 MHz bandwidth to observe the dust continuum; two windows were configured for 8 MHz bandwidth to observe para-NH<sub>2</sub>D ( $J = 1_{11} \rightarrow 1_{01}$ ) and C<sup>18</sup>O ( $J = 1 \rightarrow 0$ ); and the two remaining windows had 31 MHz bandwidth to observe <sup>13</sup>CO ( $J = 1 \rightarrow 0$ ) and <sup>12</sup>CO ( $J = 1 \rightarrow 0$ ). Two or three sources were observed per track, with further details given in Table 1. The C-configuration observations did not observe para-NH<sub>2</sub>D and another 500 MHz continuum band was allocated. Generally, we only detect <sup>12</sup>CO ( $J = 1 \rightarrow 0$ ) and the 2.9 mm continuum; there were a few weak detections in the other lines which will not be discussed further. Our root-mean-squared (RMS) sensitivity is typically 0.2 Jy beam<sup>-1</sup> channel<sup>-1</sup> for the CO ( $J = 1 \rightarrow 0$ ) and 1 mJy beam<sup>-1</sup> for the continuum data. The data were reduced, edited, and imaged using standard procedures within the MIRIAD software package (Sault et al. 1995). The uncertainty in the absolute flux is estimated to be  $\sim 20\%$ . We will only present the continuum results in this paper, the CO outflow data will be presented in an upcoming paper.

### 3. Results

The observations of  $\lambda = 2.9$  mm continuum emission enable us to probe the properties of the protostellar envelopes, in terms of mass and density profiles. We will discuss the overall flux densities, visibility amplitudes, and comparison of the visibility amplitudes to radiative transfer models. We also report the data observed toward additional sources located within our field of view, but primarily discuss the PBRS in the main text; the PBRS and non-PBRS are denoted in Table 2.

#### 3.1. Integrated 2.9 mm Dust Continuum Emission

We detect all the observed PBRS sources in the 2.9 mm continuum and deconvolved images using natural weighting are shown in Figure 1. Our observations are sensitive to spatial scales between  $\sim 1000$  AU and  $\sim 10000$  AU. On these scales, most sources have some resolved structure, in terms of extended envelope emission and in the case of HOPS 373, there is a binary source separated by  $\sim 4''$ . Two sources (082012 and 061012) also have companions  $\sim 20''$  (9400 AU) away. Images of the sources made with Robust weighting factor of -1 (Briggs 1995) did not reveal significant structure on smaller-scales. The flux densities measured from the deconvolved images are presented in Table 2. The 2.9 mm flux densities of the sample exhibit a relatively large amount of heterogeneity given the extremely red colors selection of the sample. The brightest PBRS is 082012 at 155.6 mJy and the faintest is 119019 at 10.2 mJy. Indeed, 12 of 14 PBRS have flux densities  $> 30$  mJy and their values of  $L_{\text{bol}}$  also span an order of magnitude. The combined D- and C-configuration images agree with D-configuration-only flux densities within the statistical uncertainties. Note that we also present an additional PBRS, 135003, that did not appear in ST13. This source was left out from the sample due to the  $70 \mu\text{m}$  FWHM being extended more than the cutoff value  $7''.8$ . More details of this source and its infrared and submillimeter imaging are given in the Appendix; its inclusion raises the number of PBRS in the Orion clouds to 19.

The strength of dust continuum emission from the PBRS sources prompted us to collect  $\lambda \sim 3$  mm flux densities from the literature of other Class 0 or Class I protostellar sources observed with interferometers for comparison (Table 3; Looney et al. 2000; Arce & Sargent 2006; Tobin et al. 2011)). These observations had comparable resolution and sampling of the uv-plane. To match the 2.9 mm flux densities better, we have scaled the flux densities of the comparison sources. We have done the scaling by assuming that the relative flux densities only depend on the dust opacity spectral index ( $\beta$ ) and the function  $F_\lambda \propto \lambda^{-(2+\beta)}$ . This assumption is reasonable given the similar wavelengths of the samples. With the further assumption that  $\beta \sim 1$ , the scaling factors for the 2.7 mm flux densities and 3.4 mm flux

densities are 0.8 and 1.6 respectively. We have converted all the flux densities to 2.9 mm luminosities ( $L_{2.9mm}$ ) using the distances provided in Table 3 and assuming a bandwidth of 0.11 mm (4 GHz). We plot  $L_{2.9mm}$  versus  $L_{bol}$  and the ratio of  $L_{2.9mm}$  to  $L_{bol}$  versus  $L_{bol}$  for all the data in Figure 2.

The comparison sources span the range of observed  $L_{bol}$  for the PBRs, but most PBRs have lower  $L_{bol}$  values, comparable to those in Tobin et al. (2011). They, however, have  $L_{2.9mm}$  values that are comparable to the Looney et al. (2000) sources, which are among the brightest nearby protostars a millimeter wavelengths (e.g. NGC 1333 IRAS 4A, NGC 1333 IRAS2A, IRAS 16293-2422) and are more luminous than most PBRs. Furthermore, the PBRs have among the largest values of  $L_{2.9mm}$  and  $L_{2.9mm}/L_{bol}$  ratios. This behavior is true at all luminosities, but especially evident at  $L_{bol} \sim 1 L_{\odot}$ . The non-PBRs sources in our observations generally have higher  $L_{bol}$ , higher  $T_{bol}$ , and lower  $L_{2.9mm}/L_{bol}$  ratios; however, the source HOPS 68 does intermingle with the PBRs in Figure 2. Note that the results do not significantly change whether or not scaling is applied to the literature data.

Also evident in Figure 2 is the lack of a clear relationship between  $L_{bol}$  and  $L_{2.9mm}$ . This indicates that the millimeter emission is decoupled from the central source properties (central source refers to both the protostar and accretion processes generating luminosity). The PBRs are tracing a new region of parameter space with their large amounts of circumstellar material traced by the 2.9 mm flux densities and lower values of  $L_{bol}$ .

### 3.2. Circumstellar Masses

The integrated flux densities of the protostars enable us to directly probe the circumstellar mass associated with the protostars, without significant contributions from the surrounding molecular cloud. In this case, the interferometer filtering works to our advantage by separating the envelope emission from the surrounding background cloud. To convert a flux density into a mass, we assume that the emission is optically thin and isothermal, and apply the equation

$$M = \frac{D^2 F_{\lambda}}{\kappa_{2.9mm} B_{\lambda}(T_{dust})}; \quad (1)$$

where  $B_{\lambda}$  is the Planck function. We have assumed that  $T_{dust} = 20$  K,  $\kappa_{2.9mm} = 0.00215 \text{ cm}^2 \text{ g}^{-1}$  using Ossenkopf & Henning (1994) (Table 1, Column 5) extrapolated to 2.9 mm, and  $D = 420$  pc. The extrapolation to 2.9 mm uses the dust opacity spectral index ( $\beta$ ) of the Ossenkopf & Henning (1994) dust model between 700  $\mu\text{m}$  to 1.3 mm which has  $\beta = 1.78$ . The opacity given is the dust+gas opacity, assuming a gas-to-dust ratio of 100.

The calculated masses are given in Table 2, the uncertainties given are statistical only

(not including the uncertainty in absolute flux calibration) and the masses themselves are likely only valid at the order of magnitude level given the assumptions. There may be optically thick regions of the envelope, but those are on scales of order a few hundred AU and will make only a small contribution to the overall mass.

With these assumptions, all the PBRs sources (except 119019) have more than  $1 M_{\odot}$  of surrounding material, with the largest being almost  $10 M_{\odot}$ . These masses are reflected in the high integrated flux densities observed toward these protostars. We also note that the masses are systematically larger than those calculated by ST13. The masses calculated in ST13, however, are from modified blackbody fits to the emission from  $70 \mu\text{m}$  to  $870 \mu\text{m}$  and the ST13 modified blackbody fits systematically underpredict the  $870 \mu\text{m}$  flux densities. The underprediction of the  $870 \mu\text{m}$  flux densities likely results from fitting a single temperature to data that reflect a superposition of temperatures and span an order of magnitude in wavelength. If masses were calculated directly using the  $870 \mu\text{m}$  flux, closer agreement is expected. Several non-PBRs have masses listed in Table 2 that are comparable to the mass of the PBRs. Many of these sources, however, have higher  $L_{\text{bol}}$  and  $T_{\text{bol}}$ , suggesting that the dust temperatures could be larger and by extension the masses are overestimated. We assumed  $T_{\text{dust}} = 20 \text{ K}$ , and the actual masses will be different by the ratio  $T_{\text{dust}}/20 \text{ K}$ .

The estimated masses will also change if we assume a different dust opacity law; Ossenkopf & Henning (1994) has  $\beta = 1.78$  at millimeter wavelengths (Table 1, Column 5). If we instead assume  $\beta = 1$  and use the normalization of  $0.1(\nu/1200 \text{ GHz})^{\beta}$  from Beckwith et al. (1990), the masses would be a factor of 4.5 lower.

### 3.3. Visibility Amplitudes of 2.9 mm Continuum

The integrated flux densities are only one aspect of the continuum data, the visibility amplitudes as a function of uv-distance/baseline length can reveal more about the source structure than the deconvolved images alone. We show the visibility amplitudes for all detected sources in Figure 3. How slowly (or rapidly) the amplitude decreases with increasing uv-distance reveals how concentrated the emission is toward a particular source, in addition to structural changes in the emitting material. Similar to the order of magnitude span in 2.9 mm flux density, the visibility amplitudes profiles themselves are quite varied but generally fall within two groups. About half of the observed PBRs have amplitudes that drop quickly with increasing uv-distance (HOPS 373, 082012, 302002, 119019, HOPS 372, 019003A, 061012), meaning that there is more emission on larger spatial scales relative to small spatial scales. The other half of the sample have amplitudes that are flat or slowly decreasing with increasing uv-distance (093005, 090003, 091016, 097002), indicative of most

emission arising from compact, unresolved structure. The visibility amplitudes of 082005 and 091015 are most consistent with the flat visibility amplitude sources, but decrease more rapidly than the others. We note that 135003 was only observed in D-configuration and is located in a more complex region, so it is uncertain if its flat visibilities extend toward larger uv-distances.

To examine the scales at which most flux is being emitted, we plot the ratio of the visibility amplitudes at 5 k $\lambda$  ( $\sim 41''$ , 17300 AU)  $F(5k\lambda)$  to those at 30 k $\lambda$  ( $\sim 7''$ , 3000 AU) against  $F(30k\lambda)$  and  $L_{\text{bol}}$  in Figure 4. We see that the brightest PBRs sources at 30 k $\lambda$  also have the lowest ratios, meaning that most of their flux is emitted from scales smaller than 3000 AU; 082012 is an outlier from this trend. When plotted against  $L_{\text{bol}}$ , the  $F(5k\lambda)/F(30k\lambda)$  ratio tends to be  $< 2$  for sources with luminosities of  $\sim 1 L_{\text{bol}}$ , while higher luminosity sources and non-PBRs tend to have ratios  $> 2$ . We note, however, that a source composed of just a circumstellar disk would appear to have a ratio of 1 on these plots and the non-PBRs sources that have  $F(5k\lambda)/F(30k\lambda)$  ratios  $\sim 2$  are likely more-evolved protostars whose millimeter emission is likely to be dominated by a disk on small spatial scales.

### 3.4. Comparison to Protostellar Envelope Models

The visibility amplitude profiles can also indicate the density profiles of the envelope. We ran a small grid of radiative transfer models to obtain qualitative results for the interpretation of the visibility amplitude data. The goal is to determine what density profiles are consistent with the data and if a compact, unresolved source is a necessary component for the models to fit the data. We use the Hyperion code (Robitaille 2011) to perform the radiative equilibrium calculations and produce ray-traced images of 2.9 mm continuum emission, with a  $5.0 M_{\odot}$  envelope,  $1 L_{\odot}$  central protostar, 10000 AU outer radius, and radial density profiles of  $\rho \propto R^{-1.5, -2.0, -2.5}$ , and a 50 AU radius embedded disk with  $M_{\text{disk}} = 0.0 M_{\odot}$ ,  $0.01 M_{\odot}$ , and  $0.1 M_{\odot}$ . We also ran envelope models using the density structure for a rotationally-flattened, infalling envelope (CMU envelope; Ulrich 1976; Cassen & Moosman 1981). For the CMU models, we explored the same disk masses, but we used four centrifugal radii ( $R_C = 50$  AU, 100 AU, 300 AU, and 500 AU) and assumed that the disk radius was equal to  $R_C$ ;  $R_C$  is the radius at which infalling material can be rotationally-supported due to conservation of angular momentum. The overall envelope masses of the CMU models were the same as those of the power-law envelopes. The inclination of the system only has a minor effect on the visibility amplitudes and, we assume an inclination angle of  $60^\circ$  for simplicity.

We use the dust opacities calculated by Ormel et al. (2011) for icy silicate grains and bare graphite grains grown for a period of  $3 \times 10^5$  yr. These dust opacities are similar to those

of Ossenkopf & Henning (1994) (Table 1, Column 5), but are calculated down to  $\lambda \sim 0.1 \mu\text{m}$  and include scattering properties. The dust opacity spectral index ( $\beta$ ) of the Ormel et al. (2011) models, however, is  $\sim 2$  at submillimeter and millimeter wavelengths, consistent with ISM-sized dust grains. This steep  $\beta$ , however, results in a very low dust opacity at 2.9 mm and very faint envelope emission. Therefore, we have altered the dust opacity model and at wavelengths greater than  $90 \mu\text{m}$  we transition to the Ossenkopf & Henning (1994, Table 1 Column 5) dust opacity model. This model has  $\beta \sim 1.78$ , yielding  $\kappa_{2.9\text{mm}} = 0.00215$ , producing 2.9 mm millimeter fluxes more consistent with our observations.

We could have simply increased the envelope masses such that the flux densities were consistent with our data. The Ormel et al. (2011) dust opacities, however, are a factor of 2.35 lower than Ossenkopf & Henning (1994, Table 1 Column 5). Thus, it would have been necessary to increase envelope masses to  $\sim 12 M_{\odot}$ , which may be unrealistically large for many of our sources. Furthermore, the larger masses would increase the envelope opacity at shorter wavelengths and make the overall dust temperatures lower. There is evidence for millimeter-sized dust grains in protostellar envelopes which would cause a shallower  $\beta$  of  $\sim 1$  (Sadavoy et al. 2013; Kwon et al. 2009; Schnee et al. 2014) and we therefore feel justified in adopting a hybrid dust opacity model.

We generated  $30000 \text{ AU} \times 30000 \text{ AU}$  model images with 15 AU resolution, corresponding to  $2048 \times 2048$  pixel images for emission between 2.8 mm and 3.0 mm. Such high resolution was necessary to ensure that we did not introduce false structure when Fourier transforming the images to compare with the observed visibility data. We used the MIRIAD task *fft* to calculate the Fourier transform of each model image and we azimuthally averaged the Fourier transformed image to construct a 1-dimensional visibility amplitude profile. To facilitate model comparisons, we normalized the flux densities of the envelopes and data in our comparisons at uv-distances of  $22.5 \text{ k}\lambda$ . This normalization is reasonable because most emission should be optically thin at  $\lambda \sim 3 \text{ mm}$  on spatial scales larger than our best resolution ( $\sim 2000 \text{ AU}$ ) and we are only interested in comparing the density profiles, not fitting model envelopes in detail.

We perform a simple model comparison for the sources with the best signal-to-noise ratios at the uv-distances probed by our observations: 082005, 093005, 090003, 082012, and 097002, see Figures 5 and 6. This sample is representative of the range in visibility amplitudes profiles observed, e.g., from very flat (090003, 097002, and 093005), intermediate (082005), and rapidly declining (082012).

The flat visibility amplitude sources (090003, 097002, and 093005) are consistent with a power-law envelope with  $\rho \propto R^{-2.5}$  envelope if there is no unresolved component. When a  $0.01 M_{\odot}$  unresolved component is included in a power-law envelope, the flat visibility

sources are still most consistent with a  $\rho \propto R^{-2.5}$  envelope. We note that the observed visibility amplitude profiles of 090003, 097002, and 093005 are systematically elevated with respect to the  $\rho \propto R^{-2.5}$  envelope both with and without the inclusion of a  $0.01 M_{\odot}$  disk. When comparing the flat visibility sources to models with a  $0.1 M_{\odot}$  unresolved component, all three power-law envelope density models provide a reasonable match to the visibility data since the compact source dominates the emission at uv-distances  $> 20$  k $\lambda$ , although the curvature of visibility curve of the  $R^{-1.5}$  model is opposite to that apparent in the data. In the case of the CMU envelope, the flat visibility amplitude sources are *inconsistent* with no disk component and are *consistent* with a  $0.1 M_{\odot}$  disk with  $R_C \leq 100$  AU, but the curvature of the model visibility amplitude profile is in the opposite sense as the data.

The intermediate source between the extremes of flat visibilities and rapidly declining visibilities (082005) is consistent with a density profile between  $\rho \propto R^{-2.0}$  and  $\rho \propto R^{-2.5}$  if no unresolved component is included. It is consistent with  $\rho \propto R^{-2.0}$  when a  $0.01 M_{\odot}$  unresolved component is included, but is marginally inconsistent with a power-law envelope and a  $0.1 M_{\odot}$  unresolved component. Assuming a CMU envelope, it is most consistent with  $R_C = 300$  AU and a  $0.1 M_{\odot}$  disk.

The rapidly declining visibility amplitude source 082012 is well-matched by the power-law envelope models with no unresolved component and a density profile between  $\rho \propto R^{-2.0}$  and  $\rho \propto R^{-1.5}$ . The data are also consistent with  $\rho \propto R^{-1.5}$  when a  $0.01 M_{\odot}$  disk is included. If we assume a CMU envelope structure, then 082012 is also consistent with a CMU envelope with  $R_C = 100 - 300$  AU, containing a  $0.01 M_{\odot}$  disk. Thus, sources with rapidly declining visibility amplitudes (082012 and others in the sample) are *inconsistent* with both density profiles steeper than  $\rho \propto R^{-2}$  and disk components more massive than  $0.01 M_{\odot}$ .

In addition to comparing the visibility amplitude profiles directly, we show the visibility amplitude ratios from the envelope-only models in Figure 4. These ratios can be thought of as limiting cases in the absence of a massive protostellar disk. The visibility amplitude ratio for the  $\rho \propto R^{-2.5}$  envelope is the smallest, but it is still in excess of observed sources with the smallest ratios. Most observed sources have visibility amplitude ratios in between the values found for the  $\rho \propto R^{-2.5}$  and  $\rho \propto R^{-2.0}$  models. The addition of an unresolved component to any of the models in Figure 4 would decrease the ratios, making the models more consistent with the observations, but with a shallower density profile.

The qualitative model comparison shows that multiple physical structures can be invoked to explain both the flat and rapidly declining visibility amplitude sources. The flat visibility sources can be explained with having most flux in the unresolved component or a very steep ( $\rho \propto R^{-2.5}$ ) density profile. Thus, a steep density profile is essentially indistinguishable from a compact source with our current data. The rapidly declining visibility

sources, on the other hand, are inconsistent with a massive unresolved component ( $0.1 M_{\odot}$ ) within a power-law or CMU envelope. There may, however, be some additional dependence on the disk density structure that we do not explore here. Higher resolution data will be necessary to break these degeneracies between power-law envelopes with no or an unresolved component and rotationally-flattened envelopes with a large, massive disk component.

## 4. Discussion

The PBRS represent an intriguing piece to the puzzle of low-mass star formation. Their 2.9 mm luminosities are quite large relative to their bolometric luminosities, and their millimeter luminosities are comparable to the brightest millimeter sources known in the nearby star forming regions. At the same time 4 out of the 14 observed PBRS have some of the flattest 2.9 mm visibility amplitudes observed toward any protostellar source; indeed, the most comparably flat source is NGC 1333 IRAS 4B (Looney et al. 2003). In the following subsections, we compare and contrast the PBRS to known protostars in nearby star forming regions and theoretical models to examine their significance in the star formation process as a whole.

### 4.1. Envelope Density Profiles

The favored interpretation of the the very red  $24 \mu\text{m}$  to  $70 \mu\text{m}$  colors exhibited by the PBRS is very high envelope densities (ST13). Most of the observed PBRS envelopes appear to be quite massive as measured from their 2.9 mm flux densities (Table 2). Furthermore, the low  $5 \text{ k}\lambda$  to  $30 \text{ k}\lambda$  flux ratios indicate that there is a significant amount of unresolved emission at spatial scales less than 3000 AU (in diameter) for 6 of 14 sources. Two possible explanations for the flat visibility amplitudes are either steep envelope density profiles or massive-compact structures with densities in excess of a smooth power-law density profile. Analytic protostellar collapse models predict several radial density profiles that we could expect to observe.

The Larson-Penston solution (Larson 1969) (and the numerical solution) predicts that the free-fall collapse of a constant density cloud would result in a  $\rho \propto R^{-2}$  density profile. Bonnor-Ebert spheres (Bonnor 1956) on the other hand, have a high, constant density region, with a surrounding envelope with a  $\rho \propto R^{-2}$  density profile. As a Bonnor-Ebert sphere collapses, the entire density profile approaches  $\rho \propto R^{-2}$ . A Bonnor-Ebert sphere with a small, flat inner region cannot account for the observed density structures since the density

of the inner region joins smoothly with the outer power-law envelope and our observations would require a jump to higher density. Moreover, since all the sources we observe are protostellar, we do not expect there to be a flat density region at small spatial scales.

A singular isothermal sphere (SIS) also has a  $\rho \propto R^{-2}$  density profile and this is the initial condition of the (Shu 1977) protostellar collapse model. The free-fall collapse of a SIS is inside-out, meaning there is an outwardly propagating rarefaction wave that bounds the infalling region of the envelope; the infalling region has a  $\rho \propto R^{-1.5}$  density profile. This model was extended to include rotation by Terebey et al. (1984) and the region inside the centrifugally supported radius has a density profile of  $\rho \propto R^{-0.5}$ . Within the context of these models, the envelope emission of the youngest sources is expected to be dominated by the  $\rho \propto R^{-2}$  region since both the infall and rotationally supported regions are small at early times. For an initial sound speed ( $c_s$ ) of  $0.2 \text{ km s}^{-1}$  (assuming  $T = 10 \text{ K}$ ), the infalling region would extend to a radius of  $\sim 1050 \text{ AU}$  ( $2''.5$ ) 25 kyr after collapse begins ( $r = c_s \times t$ ). Thus, for extremely young sources, one would expect that data with a maximum resolution of  $\sim 2''$  to be dominated by the  $\rho \propto R^{-2}$  component of the envelope (within the context of this model). If some of the sources, however, are more evolved, with larger collapsing regions, the shallower density profiles and possibly the rotationally-flattened portion of the density structure would be apparent in the visibility amplitudes (see Figure 6).

The envelope models that we compare to the observed visibility amplitudes in Figure 5 have density profiles that encompass those expected from the theories of protostellar collapse. Considering *only* the envelope contribution to the visibility amplitudes *without* additional unresolved source emission, however, the sources with flat visibility amplitudes (090003, 093005, 097002, 135003 and 091016) models are most consistent with the envelope density profiles that are as steep as  $\rho \propto R^{-2.5}$ . The sources with more rapidly declining visibility amplitudes (082012 and 302002) are consistent with the  $\rho \propto R^{-1.5}$  density profile. The sources in between (082005 and 091015) are consistent with  $\rho \propto R^{-2}$  density profiles. Thus, if we consider only envelopes with smooth radial density profiles, the flat visibility amplitude sources appear to be inconsistent with the analytic protostellar collapse theories, while the sources with intermediate and rapidly declining visibility amplitudes fall within theoretical expectations.

Such steep density profiles have been obtained previously toward more nearby protostars (Looney et al. 2003; Chiang et al. 2008; Kwon et al. 2009; Chiang et al. 2012). The sources with flat visibility amplitudes appear similar to NGC 1333 IRAS 4B, a source with very flat visibility amplitudes out to  $\sim 80 \text{ k}\lambda$  (Looney et al. 2003; Chiang et al. 2008); this is equivalent to flat visibility amplitudes out to  $\sim 150 \text{ k}\lambda$  at the distance to Orion. The other sources with more rapidly declining visibility amplitudes appear more similar to NGC 1333 IRAS 4A, or

IRAS 2A. Our results further confirm that the dust continuum structure of some protostellar envelopes indicate radial density profiles steeper than expected from analytic models of collapse, consistent with previous findings by Looney et al. (2003) and Kwon et al. (2009).

The density profiles steeper than the analytic models could result from having asymmetric envelope structures on these scales. Tobin et al. (2010, 2012) showed that envelopes are often filamentary and asymmetric on  $>1000$  AU scales and that infall might come through a filamentary envelope rather than a spherical envelope. The *Spitzer* IRAC and the APEX  $350\ \mu\text{m}$  and  $870\ \mu\text{m}$  images in ST13 often show filamentary structure on larger scales that may persist on smaller scales (e.g., Figures 8 and 13b of ST13). The  $2.9\ \text{mm}$  continuum images described here, however, do not have features suggestive of strong asymmetry in most cases, but Tobin et al. (2010) argued that asymmetry can be difficult to observe in the dust continuum due to the emission resulting from a combination of density and temperature.

If additional, unresolved components to the dust emission are considered (i.e., added to the envelope density profile), the flat visibility amplitude sources may be consistent with shallower density profiles. With an unresolved component of  $0.1\ M_{\odot}$ , then the  $\rho \propto R^{-2.0}$  and  $R^{-1.5}$  density profiles (in addition to  $\rho \propto R^{-2.5}$ ) are able to reproduce the flat visibility amplitudes observed for some sources (Figure 5). Even with the unresolved component, however, the curvature in the visibility amplitudes of the  $\rho \propto R^{-1.5}$  density profile is inconsistent with the data. The steeper density profiles also do not fully capture the curvature observed in the data, but the effect is less dramatic than for  $\rho \propto R^{-1.5}$ .

A circumstellar disk is a natural compact structure that is expected to develop during the star formation process (e.g., Williams & Cieza 2011, and references therein) and are likely to have a variety of sizes (Maury et al. 2010; Tobin et al. 2012). Therefore, a comparison to the CMU models with and without disk components is also of interest, see Figure 6). The rapidly declining and intermediate sources could be consistent with having a large  $R_C$  region (and a large protostellar disk), depending on the disk mass. The sources with flat visibility amplitudes can only be consistent with small  $R_C$  and a massive disk. Again, however, the curvature of the model visibility amplitude curves with small ( $R = 50\ \text{AU}$ ,  $100\ \text{AU}$ ),  $0.1\ M_{\odot}$  disks are dissimilar to that of the data. Thus, the models show that disk components are possible in the intermediate and rapidly declining cases, but the exact parameters are not well-constrained. The flat visibility amplitude sources on the other hand are grossly consistent with a disk component within the context of the CMU model, but, as stated previously, the curvature of the visibility amplitude profiles of the models relative to the observations are different.

Rather than a massive disk component, it is also possible that the envelope density profile itself is not a smooth power-law. Simulations of protostellar collapse including magnetic

fields have been shown to create density enhancements of infalling material during collapse that depart from a smooth power-law density profile (Tassis & Mouschovias 2005). Such structures can cause flattening of the visibility amplitudes due to the mass build-up at small spatial scales. The robustness of this model, however, is unclear.

Regardless of the exact nature of the structure, we can conclude that the envelopes with flat visibility amplitudes are inconsistent with the often assumed  $\rho \propto R^{-1.5}$  density profile for protostellar envelopes. The flat visibility amplitude profiles are most consistent with either a steep density profile ( $\rho \propto R^{-2.5}$ ) or the visibility amplitudes are dominated by dense, unresolved structure. The unresolved structure could be a disk, or it could be departures from a power-law density profile. Higher resolution data that resolve down to the expected scales of a disk are necessary to distinguish between these two (radically different) scenarios.

#### 4.2. Nature of the PBRs

The defining characteristic of the PBRs from the *Herschel* study by ST13 is the very red color of the PBRs sample as a whole, having  $[24\ \mu\text{m}] - [70\ \mu\text{m}]$  colors (in  $\log(\lambda F_\lambda)$  space) redder than 1.65. Furthermore, the  $T_{\text{bol}}$  measurements of the PBRs are in a narrow range of 20 - 45 K, consistent with little observed emission shortward of  $24\ \mu\text{m}$  for most PBRs. Thus, while the coldness (and redness) of the SEDs of the PBRs is consistent throughout the sample, they are very heterogeneous in terms of their ratio of  $L_{\text{submm}}$  to  $L_{\text{bol}}$  (0.6% to 6.1%),  $L_{\text{bol}}$  itself, and 2.9 mm luminosity. Nevertheless, the PBRs are characterized by higher  $L_{2.9\text{mm}}$  to  $L_{\text{bol}}$  ratios than previously identified in protostellar samples (see Figure 2).

The expected evolutionary trend for protostars is that they become more luminous as they accrete mass due to increased photospheric luminosity and greater accretion luminosity (Young & Evans 2005; Dunham et al. 2010).  $T_{\text{bol}}$  is also expected to also increase with decreasing envelope density and hence optical depth. At the same time, clearing of the envelope is likely driven by the influence of the protostellar outflow (Arce & Sargent 2006; Offner & Arce 2014). Thus, it is expected that very young Class 0 protostars will have larger millimeter flux densities (or larger envelope mass), with rather low luminosities; in other words they will have large fractions of millimeter luminosity relative to  $L_{\text{bol}}$  (e.g., Andre et al. 1993). These changes, however, may not be due solely to evolution: both initial conditions and evolution play roles in the observed  $T_{\text{bol}}$  and  $L_{\text{submm}}/L_{\text{bol}}$  ratios observed toward particular protostars (e.g. Young & Evans 2005). Further complicating matters,  $T_{\text{bol}}$  can be strongly influenced by the orientation of a given source in the plane of the sky, such that a more evolved source viewed edge-on can appear younger (ST13; Jørgensen et al.

2009; Launhardt et al. 2013; Dunham et al. 2014). Within the sample of PBRs,  $T_{\text{bol}}$  is confined to a narrow range, but there are a few sources that have low luminosities and low 2.9 mm flux densities (061012 and 119019). Meanwhile, other PBRs have both relatively high luminosities and high millimeter flux densities (082012 and HOPS 373). Such variations in the observed properties of the sample indicate that, despite the stringent color selection (ST13), the PBRs as a whole may not be characterized by a single evolutionary state. Furthermore, the fact that the PBRs present such a narrow range in  $T_{\text{bol}}$  but exhibit a broad range in other properties poses possible problems for a  $T_{\text{bol}}$ -based classification of protostars. If even at the lowest values of  $T_{\text{bol}}$  and for a uniformly selected sample we see clear variations, then even larger variations may be seen across the  $T_{\text{bol}}$  range encompassing the Class 0 and Class I protostellar phases. Thus, not all protostars of equivalent  $T_{\text{bol}}$  are equal.

With the interferometry data, we are able to determine the spatial scales from which we are detecting emission due to the high-resolution and analysis of visibility amplitude profiles. The visibility amplitude profiles of the PBRs have many features, but they can be broadly described as flat or rapidly declining. The visibility amplitude ratios from 5 k $\lambda$  to 30 k $\lambda$  (flux at  $\sim 17,000$  AU to 3000 AU scales) plotted versus 30 k $\lambda$  flux density and  $L_{\text{bol}}$  (see Figure 4), further enable the sample to be examined as a whole. The expected evolutionary trends for visibility amplitude ratios and profiles are uncertain due to the unknown contribution of the disk at a given time. Nevertheless, we can use the analytic models for protostellar envelopes as limiting cases.

If we consider the collapse of a singular isothermal sphere with a density profile  $\propto R^{-2}$ , the visibility amplitude ratios would be smaller initially and then increase as material falls in from larger radii. The density profile of the infalling region will be proportional to  $R^{-1.5}$  and this region grows with time. So, in the absence of a massive disk, the visibility amplitude ratio for such a model will be between the  $R^{-2}$  and  $R^{-1.5}$  values (see ratios taken from the models in Figure 4). Then as a disk grows and the envelope dissipates, the 5 k $\lambda$  to 30 k $\lambda$  visibility amplitude ratios will decrease (trending toward 1 on the scales examined) as the disk begins to dominate the flux density of the system at millimeter wavelengths. Thus, to summarize the visibility amplitude ratios will start small, then increase, and then decrease. The exact evolution will depend on how quickly a large disk forms and how massive such a disk is. We note that if a singular isothermal sphere formed from a Bonnor-Ebert sphere, a Bonnor-Ebert sphere would initially have a large visibility amplitude ratio, depending on the size of the flat density region (e.g., Schnee et al. 2012). The visibility amplitude ratios would then decrease as the Bonnor-Ebert sphere evolved toward a singular isothermal sphere.

Two trends are evident in the visibility amplitude ratio plots shown in Figure 4. Most of

the sources with the highest flux densities at 30 k $\lambda$  also have the lowest 5 k $\lambda$  to 30 k $\lambda$  ratios (i.e., spatially compact flux density). Then looking at the 5 k $\lambda$  to 30 k $\lambda$  ratio versus  $L_{\text{bol}}$  we see that 6 out of 14 of the lower luminosity PBRs sources ( $L_{\text{bol}} < 3 L_{\odot}$ ) have ratios between 1 and 1.5. The non-PBRs and higher luminosity PBRs tend to have higher ratios, except for the sources that are the most evolved (i.e., HOPS 223 and HOPS 59). We therefore suggest that the visibility amplitude ratios enable us to divide the PBRs sample into two groups. The PBRs with the smallest visibility amplitude ratios (flattest profiles) are the youngest of the PBRs and the sources with larger ratios (rapidly declining amplitudes) are likely more evolved, though still Class 0 protostars.

The youngest sources would then have the most compact, dense envelopes initially that may then be accreted rapidly due to the short free-fall time. The flat visibility amplitudes indicate that there is likely large amounts of mass within only a few thousand AU, implying high average densities. A source with  $2 M_{\odot}$  of envelope material a radius of 1500 AU has an average density of  $3 \times 10^7 \text{ cm}^{-3}$ , corresponding to a local free-fall time of  $\sim 10$  kyr. Thus, a substantial amount of the final protostellar mass could be accumulated in this short period of time, much less than the expected lifetime of the Class 0 phase ( $\sim 150$  kyr) (Dunham et al. 2014). Therefore, the free-fall times suggest that the Class 0 phase may begin with a short period of rapid infall that may only last  $\sim 10\%$  of the Class 0 phase. Based on the number of detected sources, ST13 suggested that if the PBRs represented a phase of protostellar evolution distinct from the Class 0 phase, it may only last  $\sim 25$  kyr. Rather than necessarily being a distinct phase, we believe that the PBRs with flat visibility amplitudes (093005, 090003, 091015, 091016, 082005, and 097002) are among the youngest Class 0 protostars, and the large amount of mass on small spatial scales could indicate that they are in a brief period of high-infall/accretion.

The PBRs that do not have flat visibility amplitudes are still young, but may be more comparable to typical Class 0 sources. We suggest that the sources with bright 2.9 mm flux densities, but rapidly declining visibility amplitudes (302002, 082012, HOPS 373) are slightly more evolved than the PBRs with flat visibility amplitudes. At least a fraction of their inner envelopes is likely to have been accreted onto the disk and/or protostar. The remaining sources with declining visibility amplitudes and low flux densities (119012, 061012, HOPS 372, 135003, 019003) are still consistent with being young Class 0 sources. Their cold  $T_{\text{bol}}$  values and extremely red 24  $\mu\text{m}$  to 70  $\mu\text{m}$ , however, colors could result from high density envelopes, but with less overall mass. Alternatively, they could be edge-on sources; we will further explore the properties of these sources in relation to their outflows in an upcoming paper (Tobin et al. in prep.).

If the proposed scenario is true, then the Class 0 phase might be a two-phase process,

with a short, rapid accretion phase (like a Bonnor-Ebert collapse; see Foster & Chevalier 1993)), lasting  $\sim 10 - 25$  kyr. This phase is then followed by a period of slower mass assembly, for the remainder of the Class 0 phase ( $\sim 100$  kyr -  $150$  kyr), assuming a Class 0 lifetime of  $\sim 160$  kyr (Dunham et al. 2014). This idea is consistent with the models of Offner & Arce (2014) that show most protostellar mass being accreted during the Class 0 phase, before the outflow destroys the envelope.

#### 4.3. Comparison to VeLLOs and candidate FSHCs

The infrared and millimeter properties of the PBRs distinguish them from typical Class 0 protostars and indicate that at least some of the PBRs may be very young Class 0 objects in a period of high infall. Two other sub-classes of protostars identified by *Spitzer* and submm/millimeter observations are the VeLLOs and candidate FHSCs and it is important to distinguish the PBRs from these sources based on their millimeter properties. First, many of the VeLLOs and candidate FHSCs are very faint at  $2.9$  mm. For instance, the brightest VeLLO/candidate FHSC at  $2.9$  mm is Per-Bolo 58 with a flux density of  $13$  mJy at  $d \sim 230$  pc (Schnee et al. 2010; Enoch et al. 2010). If this source was at the distance to Orion, it would have a flux density of only  $\sim 3.9$  mJy and only appear as a  $\sim 4\sigma$  detection in our data. This flux density is less than half that of the faintest source in the PBRs sample (119019). None of the other VeLLOs or FHSC candidates would be detectable at the distance to Orion with the sensitivity of our CARMA observations. The PBRs 061012 may be the most similar to a VeLLO, having the lowest luminosity, but it has a higher  $2.9$  mm flux density than other VeLLOs.

A comparison to the visibility amplitudes of the VeLLOs is less straightforward. Most VeLLOs/candidate FHSCs are not bright enough to enable analysis of their visibility amplitude profiles. Per-Bolo-58 is found to have rapidly declining visibility amplitudes and The candidate FHSC L1451-MMS (Pineda et al. 2011), however, has flat visibility amplitudes at  $1.3$  mm, similar to some PBRs sources. The visibility amplitudes are  $30$  mJy out to  $\sim 200$  k $\lambda$  or  $230$  AU scales. At  $2.9$  mm, the visibility amplitudes of this source would be  $2.5$  mJy, assuming  $\beta = 1$ . At the distance to Orion, however, the visibility amplitudes would be below our detection limits at  $0.8$  mJy. While the overall emitting mass of this source is much lower than the PBRs, it does have a similar  $5$  k $\lambda$  to  $30$  k $\lambda$  flux ratio, meaning that the envelope density profile might be similar to the most concentrated PBRs. However, L1451-MMS is undetected at  $70$   $\mu$ m and  $100$   $\mu$ m, unlike the PBRs. In summary, the millimeter properties of the PBRs, combined with the far-infrared constraints from ST13, distinguish the PBRs from the VeLLOs and candidate FHSCs.

## 5. Summary and Conclusions

We have presented CARMA 2.9 mm dust continuum observations toward 14 PBRs (Stutz et al. 2013) in the Orion A and B star forming regions, twelve of these protostars were first identified by *Herschel* observations. This sample of 14 PBRs also includes 135003, a new PBR that discovered by *Herschel* and was not included in the Stutz et al. (2013) sample due to their stringent FWHM cut-off. The inclusion of this source increases the total number of PBRs in Orion to 19. The PBRs classification in Stutz et al. (2013) required  $[24\mu\text{m}] - [70\mu\text{m}]$  colors or limits (in  $\log \lambda F_\lambda$  space) in excess of 1.65. In addition, we also report the continuum properties of 4 protostars and 1 apparent starless/pre-stellar core within the fields observed toward the PBRs.

All 14 PBRs are detected in dust continuum emission. Twelve out of 14 have flux densities  $> 30$  mJy and three have flux densities  $\geq 90$  mJy. The 8 PBRs with  $L_{\text{bol}} \sim 1 L_\odot$  exhibit higher 2.9 mm luminosities than other known protostars with similar  $L_{\text{bol}}$  values, and therefore have characteristics not previously identified. The PBRs with  $L_{\text{bol}} > 2.7 L_\odot$  have comparable 2.9 mm luminosities yet lower  $L_{\text{bol}}$  values than the the brightest sources in the more nearby regions of Perseus and Ophiuchus. Furthermore, the 2.9 mm luminosity does not strongly correlate with  $L_{\text{bol}}$ . This lack of correlation indicates that the 2.9 mm luminosity is not strongly dependent on either the the central protostellar luminosity or the accretion luminosity.

Six PBRs sources (097002, 090003, 093005, 082005, 091015, and 091016) have flat 2.9 mm visibility amplitudes (and 5 k $\lambda$  to 30 k $\lambda$  visibility amplitude ratios of less than 2). As a consequence, more than  $\sim 50\%$  of the total flux density arises from scales that are smaller than  $7''$  ( $\sim 3000$  AU) in diameter. This behavior indicates either steep envelope density profiles or the presence of significant mass contained within a compact, unresolved structure. We suggest that these particular PBRs are the youngest of the sample and may be in a brief period of high infall rate. Indeed, the average density on scales  $< 3000$  AU implies local free-fall times of  $\sim 10$  kyr, in agreement with independent life-time estimates based on the ratio of PBRs to protostars (Stutz et al. 2013). The PBRs with large 2.9 mm flux densities but rapidly declining visibility amplitudes (302002, 082012, HOPS 372) are still considered to be young Class 0 protostars, but may be more evolved than the PBRs with flat visibility amplitudes. The sources with lower 2.9 mm flux densities and declining visibility amplitudes (119012, 061012, HOPS 372, 135003, 019003) are also still consistent with being Class 0 sources, but may have edge-on orientations and/or lower envelope masses.

To better characterize the density profiles of the sample, we compare the observed visibility amplitudes of the sources to Hyperion radiative transfer models of axisymmetric envelopes with varying radial density profiles and unresolved components (represented by a

disk component). We also compare with rotating collapse models with various centrifugal radii and disk masses. We find that without an unresolved component to the emission, the flat visibility amplitude sources are most consistent with a  $\rho \propto R^{-2.5}$  radial density profile. If a compact structure is massive enough, however, then all three envelope density profiles tested here ( $\rho \propto R^{-1.5, -2.0, -2.5}$ ) are able to provide a reasonable match to the data. Thus, with the current data we cannot distinguish between these two scenarios and higher resolution data are required to understand the nature of these sources. Furthermore, sources with more rapidly decreasing visibility amplitudes may be consistent with shallower density profiles and are inconsistent with having a massive unresolved component.

While the PBRS occupy a narrow range to  $T_{\text{bol}}$ , their 2.9 mm flux densities and visibility amplitude profiles show a large amount of heterogeneity suggesting that they are not all in exactly the same evolutionary stage. We suggest an evolutionary trend in which the sources with flat visibility amplitude profiles are the youngest and perhaps have a dense inner envelope that may be rapidly accreted. The sources large 2.9 mm flux densities and rapidly declining visibility amplitudes may be slightly more evolved than those with flat visibility amplitudes. Moreover, the sources with flat visibility amplitude profiles also tend to have lower  $L_{\text{bol}}$  values than those with rapidly declining visibility amplitudes, consistent with the expected evolutionary trend of increasing  $L_{\text{bol}}$ . The PBRS also draw a sharp contrast with candidate FHSCs and VeLLOs. The PBRS have higher  $L_{\text{bol}}$  and larger 2.9 mm luminosities than all of the candidate FHSCs and VeLLOs; at the distance to Orion, none of the known candidate FHSCs or VeLLOs would have been confidently detected.

In summary, the PBRS have properties that are consistent with placing them among the youngest Class 0 protostars. Their millimeter and infrared properties distinguish them from typical Class 0 protostars, as well as from candidate FHSCs and VeLLOs. While the data presented here have enabled us to postulate a tentative evolutionary scenario, further characterization at higher resolutions and in molecular lines will be necessary to more firmly establish their place in the context of the star formation process.

The authors wish to thank the anonymous referee for constructive comments that improved quality and clarity of the manuscript. J.T. acknowledges support provided by NASA through Hubble Fellowship grant #HST-HF-51300.01-A awarded by the Space Telescope Science Institute, which is operated by the Association of Universities for Research in Astronomy, Inc., for NASA, under contract NAS 5-26555. J.T. also acknowledges funding from *Herschel* OT2 JPL grant #1458263. The work of A.M.S. and S.E.R. was supported by the Deutsche Forschungsgemeinschaft priority program 1573 ('Physics of the Interstellar Medium'). Support for STM and WJF was provided by NASA through awards issued by JPL/Caltech. Support for CARMA construction was derived from the states of Illinois, Cal-

ifornia, and Maryland, the James S. McDonnell Foundation, the Gordon and Betty Moore Foundation, the Kenneth T. and Eileen L. Norris Foundation, the University of Chicago, the Associates of the California Institute of Technology, and the National Science Foundation. Ongoing CARMA development and operations are supported by the National Science Foundation under a cooperative agreement, and by the CARMA partner universities. The National Radio Astronomy Observatory is a facility of the National Science Foundation operated under cooperative agreement by Associated Universities, Inc.

## A. Notes on Individual Sources

### A.1. 135003

The PBRs source 135003 is located in the OMC2/3 region of the Orion A cloud. This source was not originally included in the PBRs sample of ST13, due to it having a  $70\ \mu\text{m}$  full-width at half maximum size slightly greater than  $7''.8$ . A multi-wavelength plot of this source and its SED are given Figures 7 and 8. The  $24\ \mu\text{m}$  to  $70\ \mu\text{m}$  color ( $\log(\lambda F_\lambda(70\ \mu\text{m})/\lambda F_\lambda(24\ \mu\text{m}))$ ) for 135003 is 2.44 and it has  $L_{\text{bol}} = 11.2\ L_\odot$ ,  $T_{\text{bol}} = 34.6\ \text{K}$ ,  $L_{\text{submm}}/L_{\text{bol}} = 0.175$ , and an SED peak at  $\sim 121\ \mu\text{m}$ . These values are derived from modified blackbody fitting, the same method used in ST13. The photometry for 135003 is given in Table 4. The brighter, neighboring source is HOPS 59, a Class I protostar and separated by  $18''$  ( $\sim 7600\ \text{AU}$ ); HOPS 59 is bright both at  $2.9\ \text{mm}$  and in the infrared. There is another  $3\sigma$  source located between 135003 and HOPS 59, which may be a real source given that there is an IRAC point source detected at this position at  $3.6\ \mu\text{m}$  and  $4.5\ \mu\text{m}$ . The northeastern extension of emission from 135003 is real and has been observed in  $3\ \text{mm}$  single-dish maps of the region (Schnee et al. 2014), in addition to the  $350\ \mu\text{m}$  and  $870\ \mu\text{m}$  maps showing similarly extended structure. The visibility amplitudes of this source appear to flatten toward the longer baselines, while there is some up and down variation likely due to the extended emission and surrounding sources. Nevertheless, the overall flux density at large uv-distances is less than other PBRs.

### A.2. 093005

The reddest PBRs in  $24\ \mu\text{m}$  to  $70\ \mu\text{m}$  color, 093005, is located at the intersection of three filaments and  $\sim 110''$  north of its nearby neighbor of HOPS 373 (ST13). At wavelengths shorter than  $70\ \mu\text{m}$ , 093005 was only detected in *Spitzer*  $4.5\ \mu\text{m}$  imaging (ST13). The dust continuum emission from this source is quite compact, only  $\sim 1.2\times$  fainter at  $30\ \text{k}\lambda$  versus  $5$

$k\lambda$  and the visibility amplitudes are very flat out to  $\sim 80 k\lambda$ .

### A.3. HOPS 373

HOPS 373 is the close neighbor of 093005, located  $110''$  to the south. The dust continuum emission observed in D-configuration only showed some asymmetry and the combined D and C configuration data resolve a second component, separated by  $4''$ . The continuum emission from HOPS 373 is fainter than 093005 and the visibility amplitudes fall quickly with increasing uv-distance, reaching zero at  $50 k\lambda$  and then rise again, showing the expected pattern for two sources separated by  $4''$ .

### A.4. 090003

The PBRs 090003 (also called Orion B9 SMM 3; Miettinen et al. (2012)) is located in a loose filamentary complex with several protostars and starless cores over a  $0.5 pc$  region (Miettinen et al. 2012). Much like 093005, its only detection shortward of  $24 \mu m$  is at  $4.5 \mu m$ , where there is a small feature offset from the location of the protostar, indicative of shocked  $H_2$  emission (Miettinen et al. 2012; Stutz et al. 2013).

The envelope as observed at  $870 \mu m$  is extended to the east and at  $350 \mu m$  there are a few sub-peaks associated with the extended  $870 \mu m$  emission (Miettinen et al. 2012). We do not, however, detect  $2.9 mm$  continuum emission from these sub-peaks, indicating that they do not harbor compact protostellar sources. The continuum emission from 090003 has a very similar visibility amplitude profile to 093005, indicating that this source is also dominated by small-scale emission. The source 090003 is the second brightest in the sample at  $2.9 mm$ .

### A.5. 082012 and HOPS 372

The brightest continuum source in the sample is 082012; the  $2.9 mm$  continuum luminosity of 082012 is about the same as that of the well-studied multiple protostellar system IRAS 16293-2422. Similarly, 082012 has visibility amplitudes that are falling quickly as a function of uv-distance, indicating that the source is not dominated by compact emission. Moreover, 082012 ( $L_{bol} = 6.3 L_{\odot}$ ) has a lower luminosity than other protostars with similar envelope characteristics. Only  $\sim 20''$  away from 082012 is HOPS 372, another PBRs source, but with much lower overall continuum flux.

### A.6. 019003

The PBRS source 019003 is also located in the OMC 2/3 region, northward of 135003. We detect four sources at 2.9 mm surrounding 019003 (Figure 1): HOPS 71 farthest to the east, HOPS 68 to the south, and 019003 itself, which resolves into two sources denoted 019003 A and 019003 B. The source 019003 A is most closely associated with the 70  $\mu\text{m}$  source detected by ST13. The 70  $\mu\text{m}$  source, however, is offset by  $\sim 3''$  to the west, as are the 4.5  $\mu\text{m}$  and 24  $\mu\text{m}$  sources. On the other hand, 019003 B appears to be starless, with no detections at any wavelength shorter than 160  $\mu\text{m}$ .

### A.7. HOPS 68

The protostar HOPS 68 is detected at the edge of the 019003 field. This source was previously recognized for the appearance of crystalline silicates in its *Spitzer* IRS spectrum (Poteet et al. 2011).

### A.8. 302002

The source 302002 is located at the end of an isolated filamentary structure in NGC 2068,  $\sim 20''$  to the south of a Class I source (HOPS 331). The 2.9 mm continuum is well-detected toward 302002, whereas HOPS 331 is undetected. The visibility amplitudes toward this source are falling with increasing uv-distance, similar to those of 082012.

### A.9. 061012 and HOPS 223

The source 061012 is located very near the outbursting protostar V2775 Ori (HOPS 223; also detected at 2.9 mm) in the L1641 region (Fischer et al. 2012). This source is one of the faintest PBRS in the sample at 17 mJy; indeed, only 119019 is slightly fainter. The visibility amplitudes appear rather flat, but become dominated by noise at uv-distances larger than 20 k $\lambda$ . Hence, its nature is uncertain.

#### A.10. 091015 and 091016

The two sources 091015 and 091016 are close neighbors in NGC 2068, the former being  $\sim 40''$  west of the latter. These sources are completely undetected at wavelengths shortward of  $70\ \mu\text{m}$ . The visibility amplitudes are flat across all observed uv-distances toward both sources in Figure 3, with 091015 declining a bit more rapidly than 091016.

#### A.11. 082005

The source 082005 is located about  $4'$  south of 082012, and these sources are connected by an apparent filamentary structure seen at  $160\ \mu\text{m}$  and  $870\ \mu\text{m}$ . This source is also undetected at wavelengths shorter than  $70\ \mu\text{m}$ , like 091015 and 091016. The visibility amplitude data for the dust continuum are rather flat like some of the other deeply embedded sources, but still decline more rapidly than the flattest sources.

#### A.12. 097002

The source 097002 is found near a bright  $4.5\ \mu\text{m}$  and  $24\ \mu\text{m}$  source seen in *Spitzer* data, as shown by ST13. At  $70\ \mu\text{m}$ , the neighboring  $24\ \mu\text{m}$  source is undetected, but 097002 is quite apparent. We detect 097002 as a bright  $2.9\ \text{mm}$  continuum source with very flat visibility amplitudes, but we do not detect the neighboring source. Much like 090003 and 093005, the visibility amplitudes toward this source are very flat.

#### A.13. 119019

The source 119019 is the faintest PBRs source in terms of  $2.9\ \text{mm}$  continuum emission and appears more similar to the protostars observed in the Tobin et al. (2011) sample rather than the PBRs sources.

### REFERENCES

- Ali, B., Tobin, J. J., Fischer, W. J., Poteet, C. A., Megeath, S. T., Allen, L., Hartmann, L., Calvet, N., Furlan, E., & Osorio, M. 2010, *A&A*, 518, L119
- Andre, P., Ward-Thompson, D., & Barsony, M. 1993, *ApJ*, 406, 122

- Arce, H. G., & Sargent, A. I. 2006, *ApJ*, 646, 1070
- Beckwith, S. V. W., Sargent, A. I., Chini, R. S., & Guesten, R. 1990, *AJ*, 99, 924
- Bonnor, W. B. 1956, *MNRAS*, 116, 351
- Bourke, T. L., Myers, P. C., Evans, II, N. J., Dunham, M. M., Kauffmann, J., Shirley, Y. L., Crapsi, A., Young, C. H., Huard, T. L., Brooke, T. Y., Chapman, N., Cieza, L., Lee, C. W., Teuben, P., & Wahhaj, Z. 2006, *ApJ*, 649, L37
- Briggs, D. S. 1995, in *Bulletin of the American Astronomical Society*, Vol. 27, American Astronomical Society Meeting Abstracts, 112.02
- Cassen, P., & Moosman, A. 1981, *Icarus*, 48, 353
- Chen, X., Arce, H. G., Zhang, Q., Bourke, T. L., Launhardt, R., Schmalzl, M., & Henning, T. 2010, *ApJ*, 715, 1344
- Chiang, H., Looney, L. W., Tassis, K., Mundy, L. G., & Mouschovias, T. C. 2008, *ApJ*, 680, 474
- Chiang, H., Looney, L. W., & Tobin, J. J. 2012, *ApJ*, 709, 470
- Commerçon, B., Launhardt, R., Dullemond, C., & Henning, T. 2012, *A&A*, 545, A98
- Dunham, M. M., Crapsi, A., Evans, II, N. J., Bourke, T. L., Huard, T. L., Myers, P. C., & Kauffmann, J. 2008, *ApJS*, 179, 249
- Dunham, M. M., Evans, N. J., Terebey, S., Dullemond, C. P., & Young, C. H. 2010, *ApJ*, 710, 470
- Dunham, M. M., Stutz, A. M., Allen, L. E., Evans, II, N. J., Fischer, W. J., Megeath, S. T., Myers, P. C., Offner, S. S. R., Poteet, C. A., Tobin, J. J., & Vorobyov, E. I. 2014, *ArXiv e-prints*
- Enoch, M. L., Lee, J.-E., Harvey, P., Dunham, M. M., & Schnee, S. 2010, *ApJ*, 722, L33
- Fischer, W. J., Megeath, S. T., Ali, B., Tobin, J. J., Osorio, M., Allen, L. E., Kryukova, E., Stanke, T., Stutz, A. M., Bergin, E., Calvet, N., di Francesco, J., Furlan, E., Hartmann, L., Henning, T., Krause, O., Manoj, P., Maret, S., Muzerolle, J., Myers, P., Neufeld, D., Pontoppidan, K., Poteet, C. A., Watson, D. M., & Wilson, T. 2010, *A&A*, 518, L122
- Fischer, W. J., Megeath, S. T., Tobin, J. J., Stutz, A. M., Ali, B., Remming, I., Kounkel, M., Stanke, T., Osorio, M., Henning, T., Manoj, P., & Wilson, T. L. 2012, *ApJ*, 756, 99
- Foster, P. N., & Chevalier, R. A. 1993, *ApJ*, 416, 303
- Johnstone, D., & Bally, J. 1999, *ApJ*, 510, L49
- Jørgensen, J. K., van Dishoeck, E. F., Visser, R., Bourke, T. L., Wilner, D. J., Lommen, D., Hogerheijde, M. R., & Myers, P. C. 2009, *A&A*, 507, 861

- Keene, J., Davidson, J. A., Harper, D. A., Hildebrand, R. H., Jaffe, D. T., Loewenstein, R. F., Low, F. J., & Pernic, R. 1983, *ApJ*, 274, L43
- Kryukova, E., Megeath, S. T., Gutermuth, R. A., Pipher, J., Allen, T. S., Allen, L. E., Myers, P. C., & Muzerolle, J. 2012, *AJ*, 144, 31
- Kwon, W., Looney, L. W., Mundy, L. G., Chiang, H.-F., & Kemball, A. J. 2009, *ApJ*, 696, 841
- Larson, R. B. 1969, *MNRAS*, 145, 271
- Launhardt, R., Stutz, A. M., Schmiedeke, A., Henning, T., Krause, O., Balog, Z., Beuther, H., Birkmann, S., Hennemann, M., Kainulainen, J., Khanzadyan, T., Linz, H., Lippok, N., Nielbock, M., Pitann, J., Ragan, S., Risacher, C., Schmalzl, M., Shirley, Y. L., Stecklum, B., Steinacker, J., & Tackenberg, J. 2013, *A&A*, 551, A98
- Looney, L. W., Mundy, L. G., & Welch, W. J. 2000, *ApJ*, 529, 477
- . 2003, *ApJ*, 592, 255
- Manoj, P., Watson, D. M., Neufeld, D. A., Megeath, S. T., Vavrek, R., Yu, V., Visser, R., Bergin, E. A., Fischer, W. J., Tobin, J. J., Stutz, A. M., Ali, B., Wilson, T. L., Di Francesco, J., Osorio, M., Maret, S., & Poteet, C. A. 2013, *ApJ*, 763, 83
- Maury, A. J., André, P., Hennebelle, P., Motte, F., Stamatellos, D., Bate, M., Belloche, A., Duchêne, G., & Whitworth, A. 2010, *A&A*, 512, A40+
- Megeath, S. T., Gutermuth, R., Muzerolle, J., Kryukova, E., Flaherty, K., Hora, J. L., Allen, L. E., Hartmann, L., Myers, P. C., Pipher, J. L., Stauffer, J., Young, E. T., & Fazio, G. G. 2012, *AJ*, 144, 192
- Miettinen, O., Harju, J., Haikala, L. K., & Juvela, M. 2012, *A&A*, 538, A137
- Motte, F., & André, P. 2001, *A&A*, 365, 440
- Myers, P. C., & Ladd, E. F. 1993, *ApJ*, 413, L47
- Offner, S. S. R., & Arce, H. G. 2014, *ApJ*, 784, 61
- Ormel, C. W., Min, M., Tielens, A. G. G. M., Dominik, C., & Paszun, D. 2011, *A&A*, 532, A43
- Ossenkopf, V., & Henning, T. 1994, *A&A*, 291, 943
- Pineda, J. E., Arce, H. G., Schnee, S., Goodman, A. A., Bourke, T., Foster, J. B., Robitaille, T., Tanner, J., Kauffmann, J., Tafalla, M., Caselli, P., & Anglada, G. 2011, *ApJ*, 743, 201

- Polychroni, D., Schisano, E., Elia, D., Roy, A., Molinari, S., Martin, P., André, P., Turrini, D., Rygl, K. L. J., Di Francesco, J., Benedettini, M., Busquet, G., di Giorgio, A. M., Pestalozzi, M., Pezzuto, S., Arzoumanian, D., Bontemps, S., Hennemann, M., Hill, T., Könyves, V., Men'shchikov, A., Motte, F., Nguyen-Luong, Q., Peretto, N., Schneider, N., & White, G. 2013, *ApJ*, 777, L33
- Poteet, C. A., Megeath, S. T., Watson, D. M., Calvet, N., Remming, I. S., McClure, M. K., Sargent, B. A., Fischer, W. J., Furlan, E., Allen, L. E., Bjorkman, J. E., Hartmann, L., Muzerolle, J., Tobin, J. J., & Ali, B. 2011, *ApJ*, 733, L32
- Ragan, S., Henning, T., Krause, O., Pitann, J., Beuther, H., Linz, H., Tackenberg, J., Balog, Z., Hennemann, M., Launhardt, R., Lippok, N., Nielbock, M., Schmiedeke, A., Schuller, F., Steinacker, J., Stutz, A., & Vasyunina, T. 2012, *A&A*, 547, A49
- Robitaille, T. P. 2011, *A&A*, 536, A79
- Sadavoy, S. I., Di Francesco, J., Johnstone, D., Currie, M. J., Drabek, E., Hatchell, J., Nutter, D., André, P., Arzoumanian, D., Benedettini, M., Bernard, J.-P., Duarte-Cabral, A., Fallscheer, C., Friesen, R., Greaves, J., Hennemann, M., Hill, T., Jenness, T., Könyves, V., Matthews, B., Mottram, J. C., Pezzuto, S., Roy, A., Rygl, K., Schneider-Bontemps, N., Spinoglio, L., Testi, L., Tothill, N., Ward-Thompson, D., White, G., JCMT, t., & Herschel Gould Belt Survey Teams. 2013, *ApJ*, 767, 126
- Sault, R. J., Teuben, P. J., & Wright, M. C. H. 1995, in *Astronomical Society of the Pacific Conference Series*, Vol. 77, *Astronomical Data Analysis Software and Systems IV*, ed. R. A. Shaw, H. E. Payne, & J. J. E. Hayes, 433–+
- Schnee, S., Di Francesco, J., Enoch, M., Friesen, R., Johnstone, D., & Sadavoy, S. 2012, *ApJ*, 745, 18
- Schnee, S., Enoch, M., Johnstone, D., Culverhouse, T., Leitch, E., Marrone, D. P., & Sargent, A. 2010, *ApJ*, 718, 306
- Schnee, S., Mason, B., Di Francesco, J., Friesen, R., Li, D., Sadavoy, S., & Stanke, T. 2014, *ArXiv e-prints*
- Shu, F. H. 1977, *ApJ*, 214, 488
- Stanke, T., Stutz, A. M., Tobin, J. J., Ali, B., Megeath, S. T., Krause, O., Linz, H., Allen, L., Bergin, E., Calvet, N., di Francesco, J., Fischer, W. J., Furlan, E., Hartmann, L., Henning, T., Manoj, P., Maret, S., Muzerolle, J., Myers, P. C., Neufeld, D., Osorio, M., Pontoppidan, K., Poteet, C. A., Watson, D. M., & Wilson, T. 2010, *A&A*, 518, L94
- Stutz, A., Launhardt, R., Linz, H., Krause, O., Henning, T., Kainulainen, J., Nielbock, M., Steinacker, J., & André, P. 2010, *A&A*, 518, L87

- Stutz, A. M., Rubin, M., Werner, M. W., Rieke, G. H., Biegging, J. H., Keene, J., Kang, M., Shirley, Y. L., Su, K. Y. L., Velusamy, T., & Wilner, D. J. 2008, *ApJ*, 687, 389
- Stutz, A. M., Tobin, J. J., Stanke, T., Megeath, S. T., Fischer, W. J., Robitaille, T., Henning, T., Ali, B., di Francesco, J., Furlan, E., Hartmann, L., Osorio, M., Wilson, T. L., Allen, L., Krause, O., & Manoj, P. 2013, *ApJ*, 767, 36
- Tassis, K., & Mouschovias, T. C. 2005, *ApJ*, 618, 783
- Terebey, S., Shu, F. H., & Cassen, P. 1984, *ApJ*, 286, 529
- Tobin, J. J., Hartmann, L., Chiang, H.-F., Looney, L. W., Bergin, E. A., Chandler, C. J., Masqué, J. M., Maret, S., & Heitsch, F. 2011, *ApJ*, 740, 45
- Tobin, J. J., Hartmann, L., Chiang, H.-F., Wilner, D. J., Looney, L. W., Loinard, L., Calvet, N., & D’Alessio, P. 2012, *Nature*, 492, 83
- Tobin, J. J., Hartmann, L., Looney, L. W., & Chiang, H.-F. 2010, *ApJ*, 712, 1010
- Ulrich, R. K. 1976, *ApJ*, 210, 377
- Williams, J. P., & Cieza, L. A. 2011, *ArXiv e-prints*
- Young, C. H., & Evans, II, N. J. 2005, *ApJ*, 627, 293

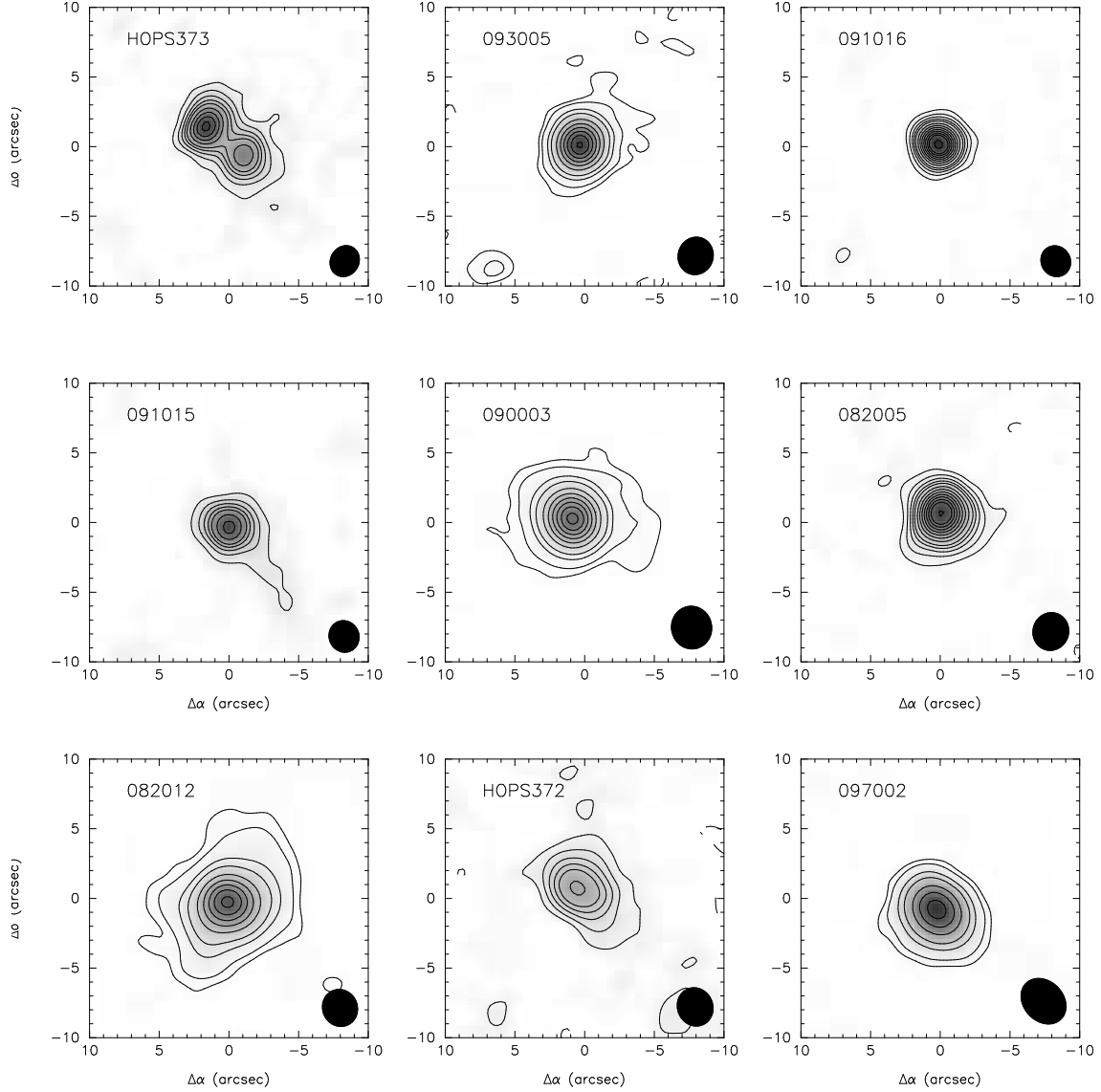


Fig. 1.— Continuum images at 2.9 mm for the observed PBRs sample and sources within the field of view. While many appear mostly round, some have marginally resolved emission and Table 3 shows that the peak flux densities are less than the integrated flux densities. The sources in Figure 1a are a combination of D and C configuration data and the sources with only D-configuration data are shown in Figure 1b. The contours are  $[-3, 3, 6, 9, 12, 15, 20, 25, 30, 35, 40, 45, 50, 60, \dots] \times \sigma$  for all sources except 093005, 090003, and 082012 where the contours are  $[-3, 3, 6, 15, 25, 45, 65, 85, \dots] \times \sigma$ ;  $\sigma$  is given for each source in Table 2.

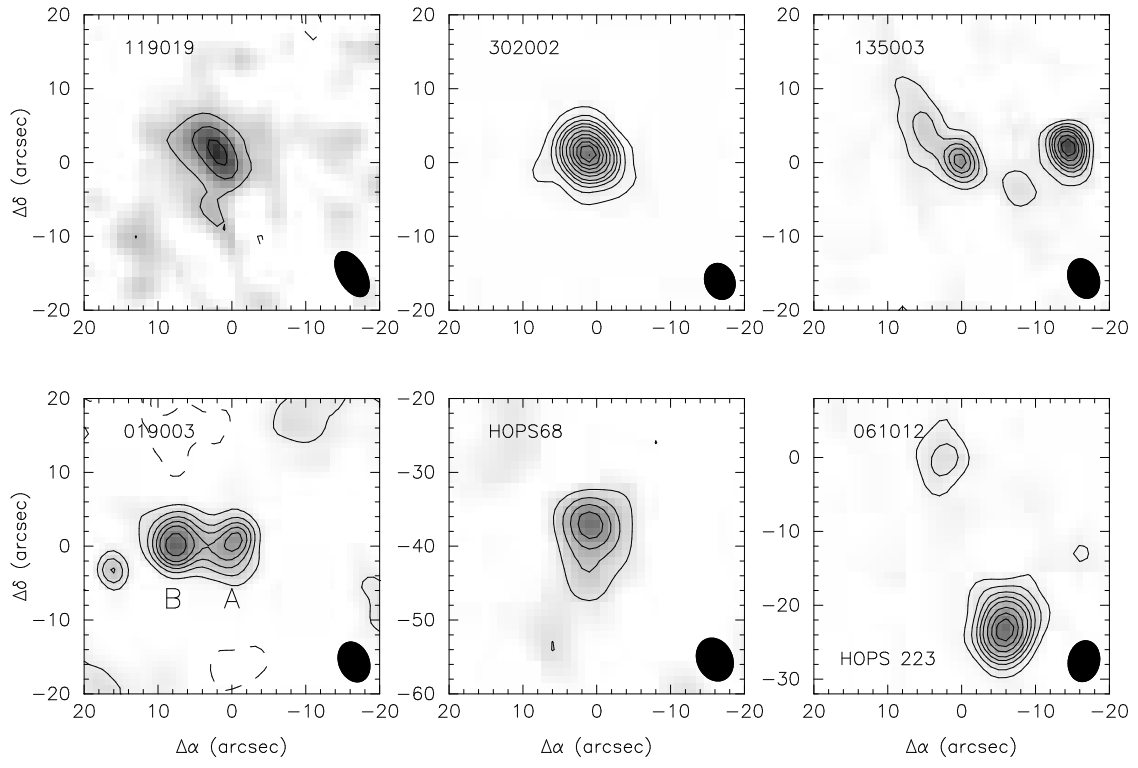


Fig. 1b.—

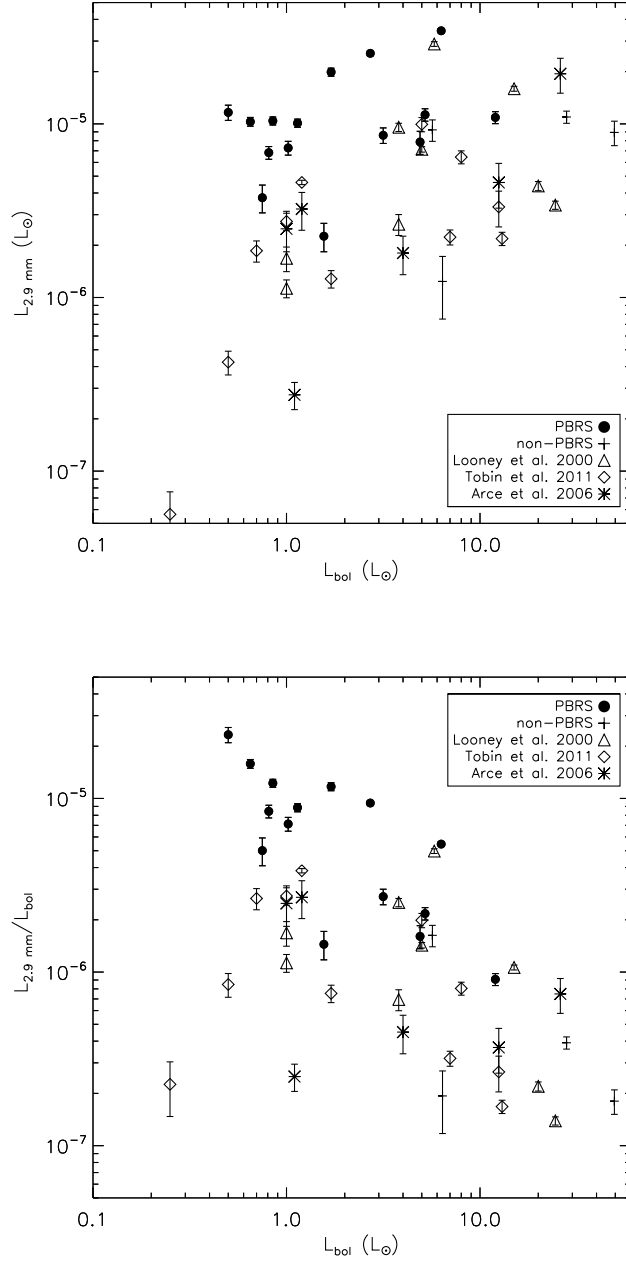


Fig. 2.— Plots of the 2.9 mm luminosity ( $L_{2.9\text{mm}}$ ) versus  $L_{\text{bol}}$  (top) and the  $L_{2.9\text{mm}}/L_{\text{bol}}$  ratio versus  $L_{\text{bol}}$  (bottom). We also include sources observed by Tobin et al. (2011) at 3.4 mm, by Looney et al. (2000) at 2.7 mm, and by Arce & Sargent (2006) at 2.7 mm. For luminosities of about  $1 L_{\odot}$ , the PBRs have the highest 2.9 mm luminosity ratios and at higher luminosities they are comparable to or larger than those from Looney et al. (2000). Note that we have rescaled the flux densities from the literature to account for the spectral slopes, assuming  $\beta = 1$ , the 3.4 mm flux densities are increased by a factor of 1.6 and the 2.7 mm flux densities are decreased by a factor of 0.8. Note that the scaling does not affect the result of the PBRs having among the highest  $L_{2.9\text{mm}}$  values for a given  $L_{\text{bol}}$ .

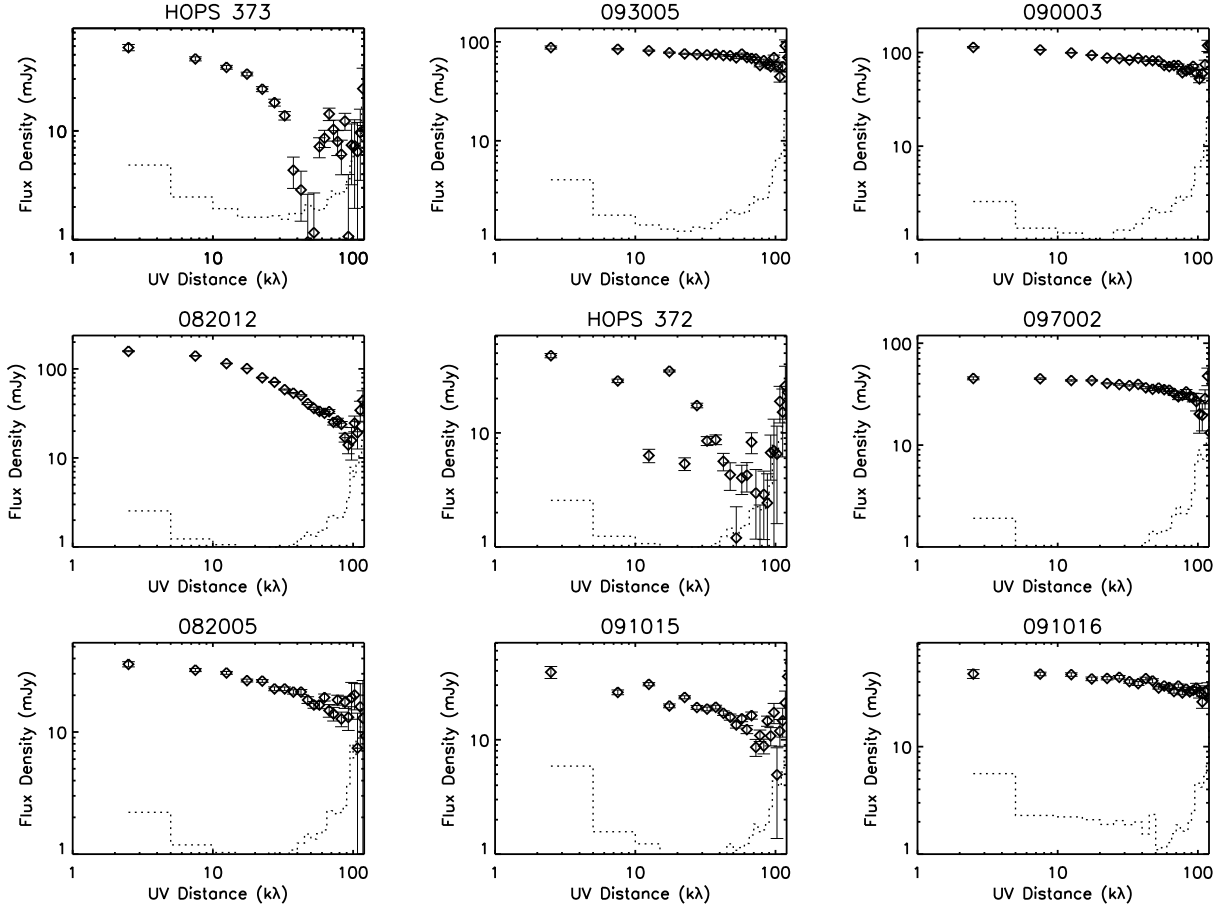


Fig. 3.— Visibility amplitude versus uv-distance plots for all the sources. Flatter visibility amplitudes with increasing projected uv-distance indicate that the flux density is dominated by compact, unresolved emission (e.g., 093005, 090003, 082005, 091015, 091016). Visibility amplitudes that are decreasing rapidly with increased uv-distance indicate that there is more flux on larger spatial scales, relative to a compact unresolved component (e.g., 082012, 302002, HOPS 373, HOPS 223). The light dashed line in each plot is the expected visibility amplitude that would be measured from noise alone. Sources only observed in D-configuration with shorter uv-distances are shown in Figure 3b.

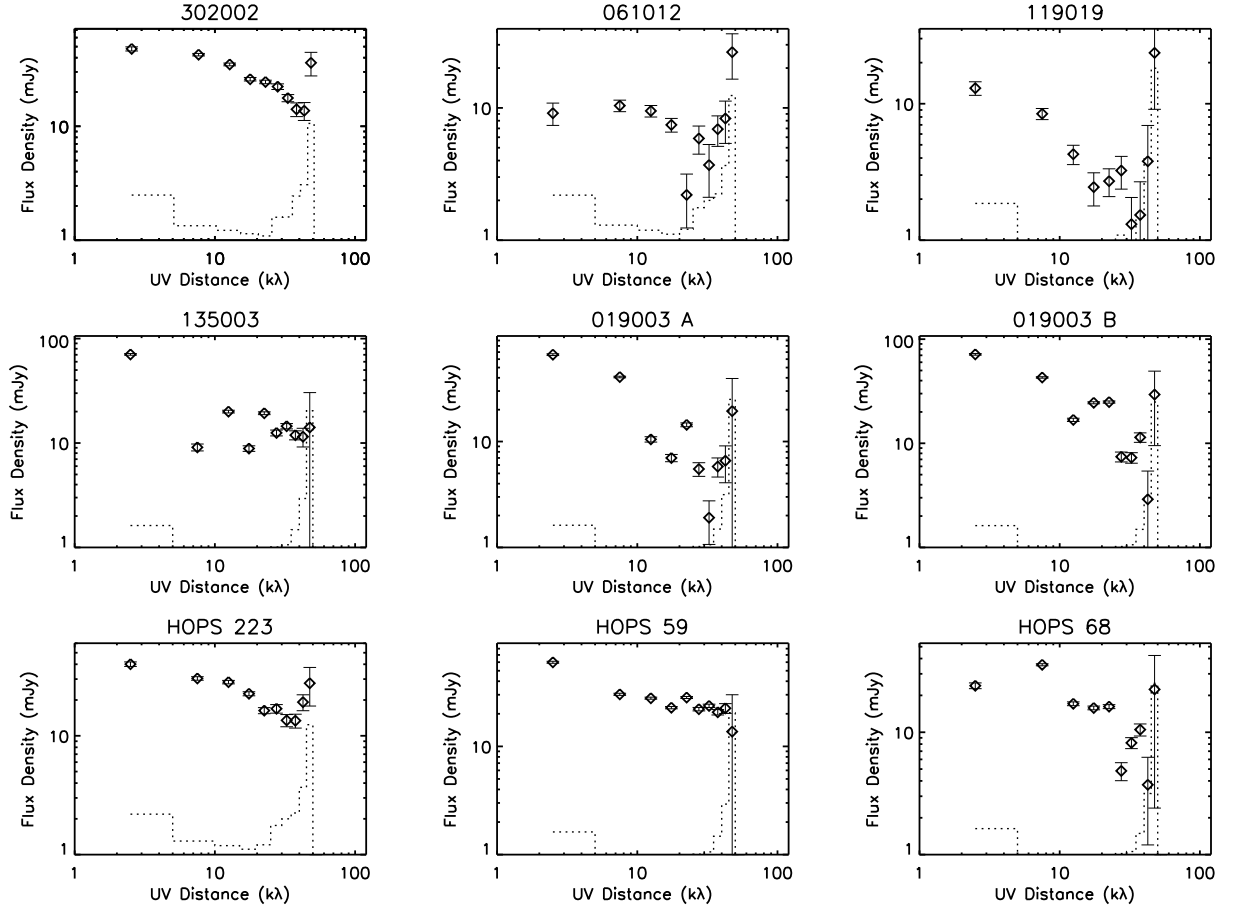


Fig. 3b.—

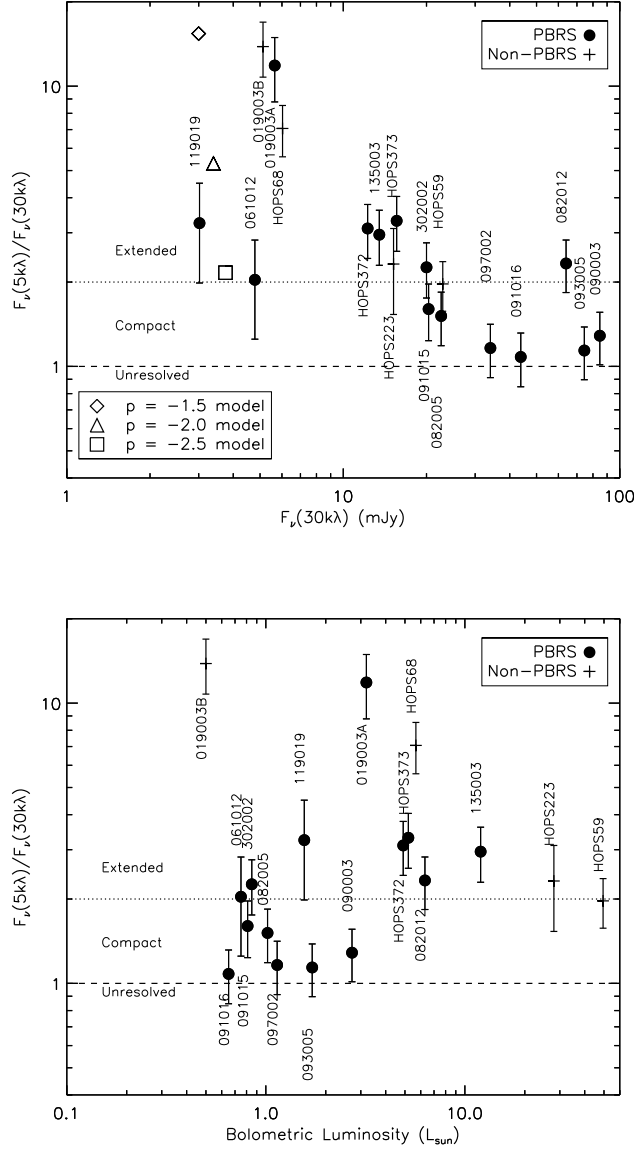


Fig. 4.— Plot of the flux density ratio at 5 kλ and 30 kλ to the flux density at 30 kλ (top) and a plot of  $L_{\text{bol}}$  versus the flux density ratio at 5 kλ and 30 kλ versus  $L_{\text{bol}}$  (bottom). The higher the ratio, the more flux is resolved out at the larger uv-distances. This plot enables us to separate the PBRS and other protostars into two groups, one with low flux ratios, meaning that most emission is from small spatial scales and the other where most emission is from larger spatial scales. There is a trend for the lower luminosity PBRS to have lower 5 kλ to 30 kλ flux ratios, while more luminous sources have higher ratios. The fine dotted line is for a 5 kλ to 30 kλ flux ratio of 2, about the limit where sources significantly deviate from a flat appearance in Figure 3 and the dashed line simply is a flux density ratio of unity for reference. Ratios from model envelopes with density profiles proportional to  $R^{-p}$  where  $p = -1.5, -2.0$ , and  $-2.5$  are shown in the top panel as a diamond, triangle, and square, respectively.

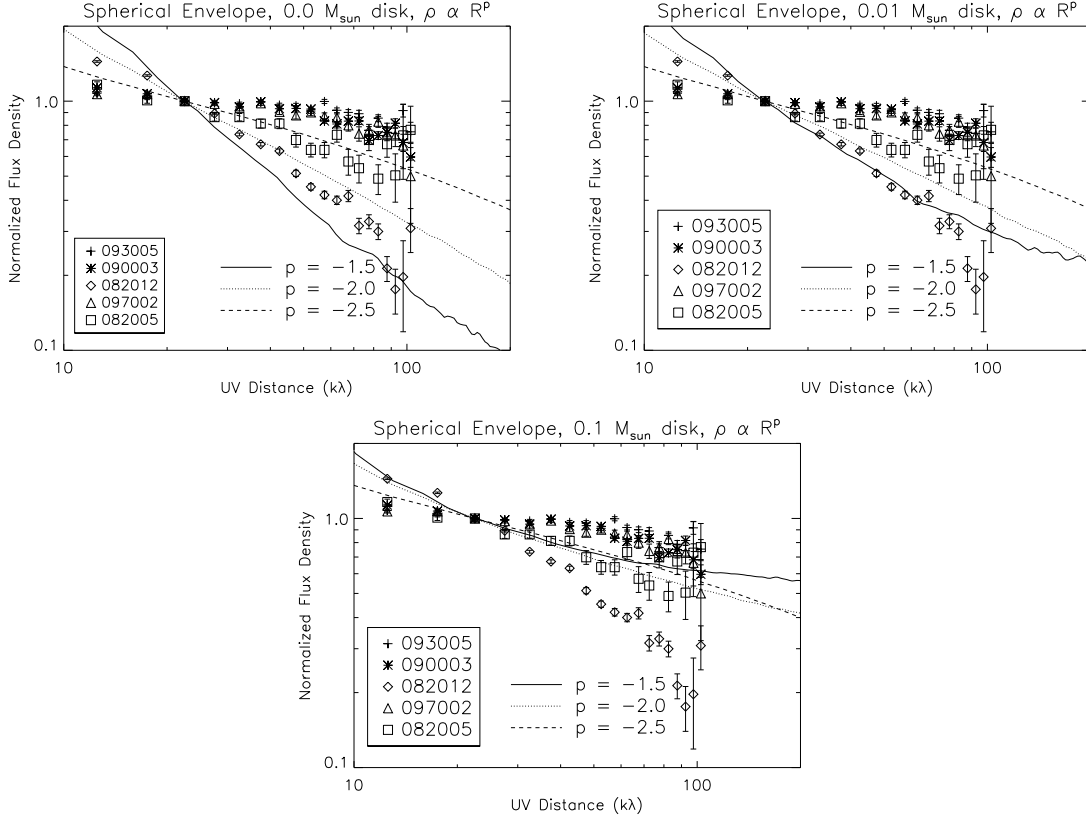


Fig. 5.— Plots of normalized visibility amplitudes versus uv-distance for models and a few representative sources overlaid. We plot radial density profiles ( $\rho \propto R^{-1.5, -2.0, -2.5}$ ) and compact object (disk) masses of  $0.0 M_{\odot}$ ,  $0.01 M_{\odot}$ , and  $0.1 M_{\odot}$  in each plot. The flux densities are normalized at  $22.5 k\lambda$  ( $9.2''$ ;  $3850 \text{ AU}$ ) to limit the contribution of flux external to the envelopes and only probe internal structure. With no compact structure (i.e., no disk), the sources with flat visibility amplitudes are consistent with either having a density profile as steep as  $\rho \propto R^{-2.5}$  or being dominated by unresolved structure, while 082012 is inconsistent with being dominated by unresolved structure.

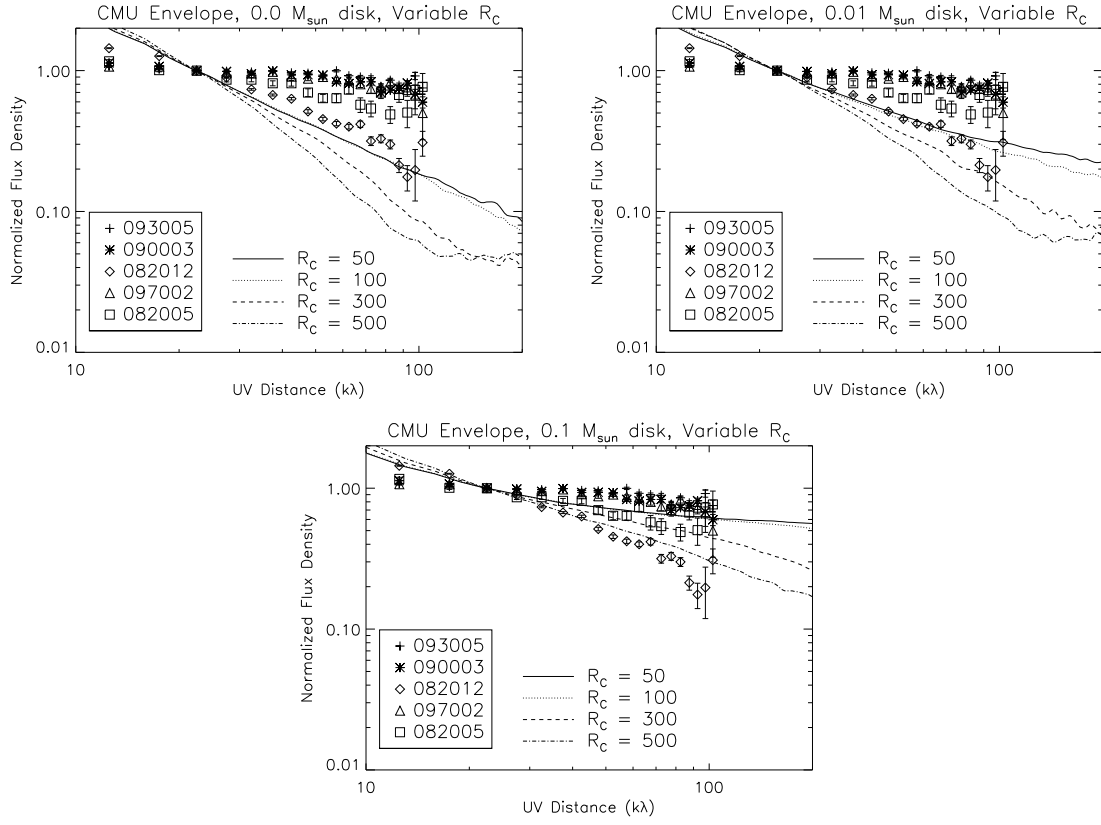


Fig. 6.— Same as Figure 5, but for CMU, rotationally flattened envelopes with various centrifugal radii.

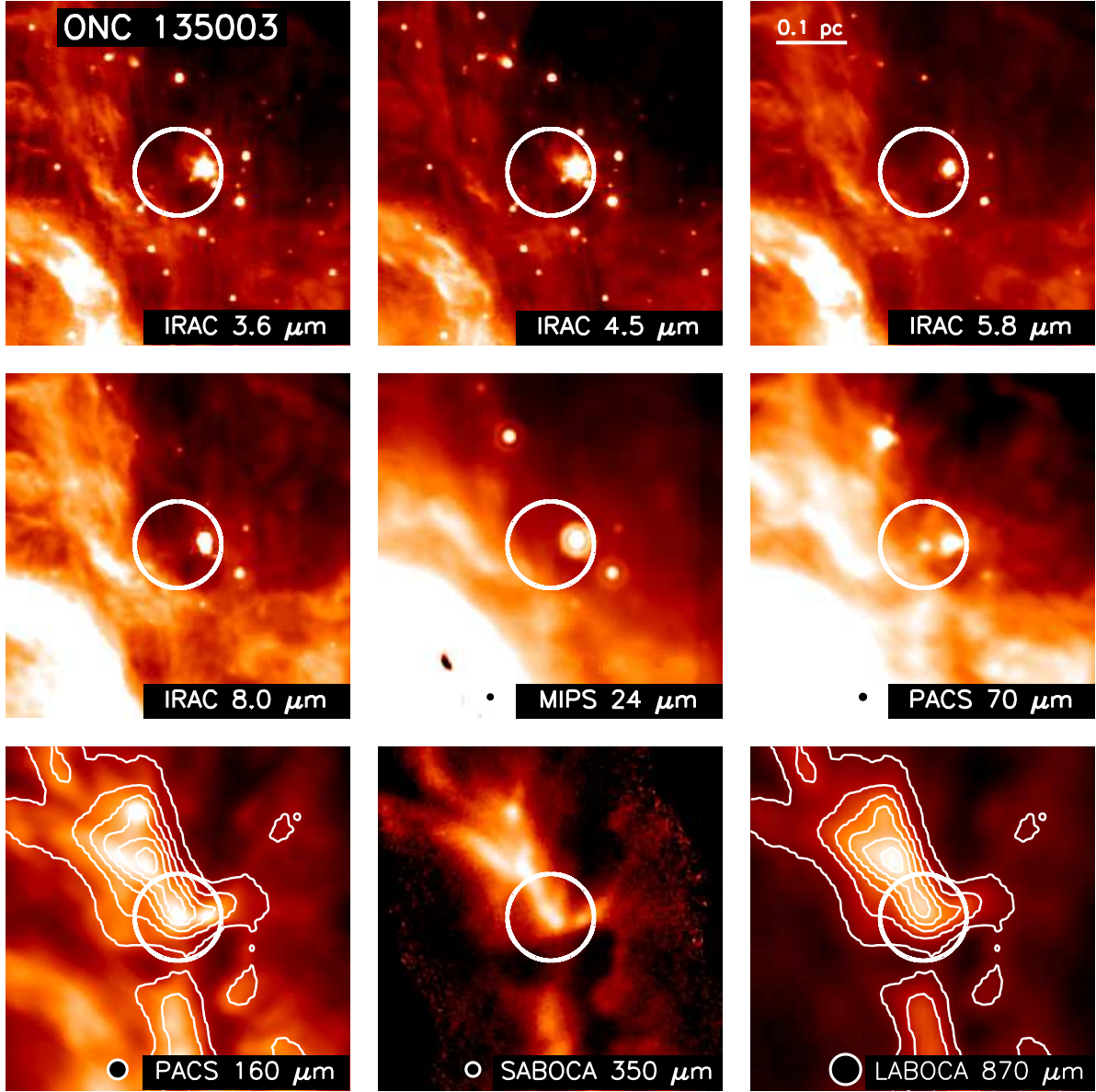


Fig. 7.— Multi-wavelength images of the additional PBRs source 135003. This source is located in the OMC 2/3 region where there are high levels of nebosity. The source immediately west of 135003 is HOPS 59, a Class I protostar. Notice that 135003 resides at an inflection point of the filament traced at longer wavelengths. The white circle marks the location of 135003 and is  $30''$  in radius. The black circles at the bottom are the respective beam sizes. The contours overlaid on the  $160\ \mu\text{m}$  and  $870\ \mu\text{m}$  images are the  $870\ \mu\text{m}$  emission contours at  $[0.5, 1.0, 1.5, 2.0, 2.5, \text{ and } 3.0]\ \text{Jy beam}^{-1}$ .

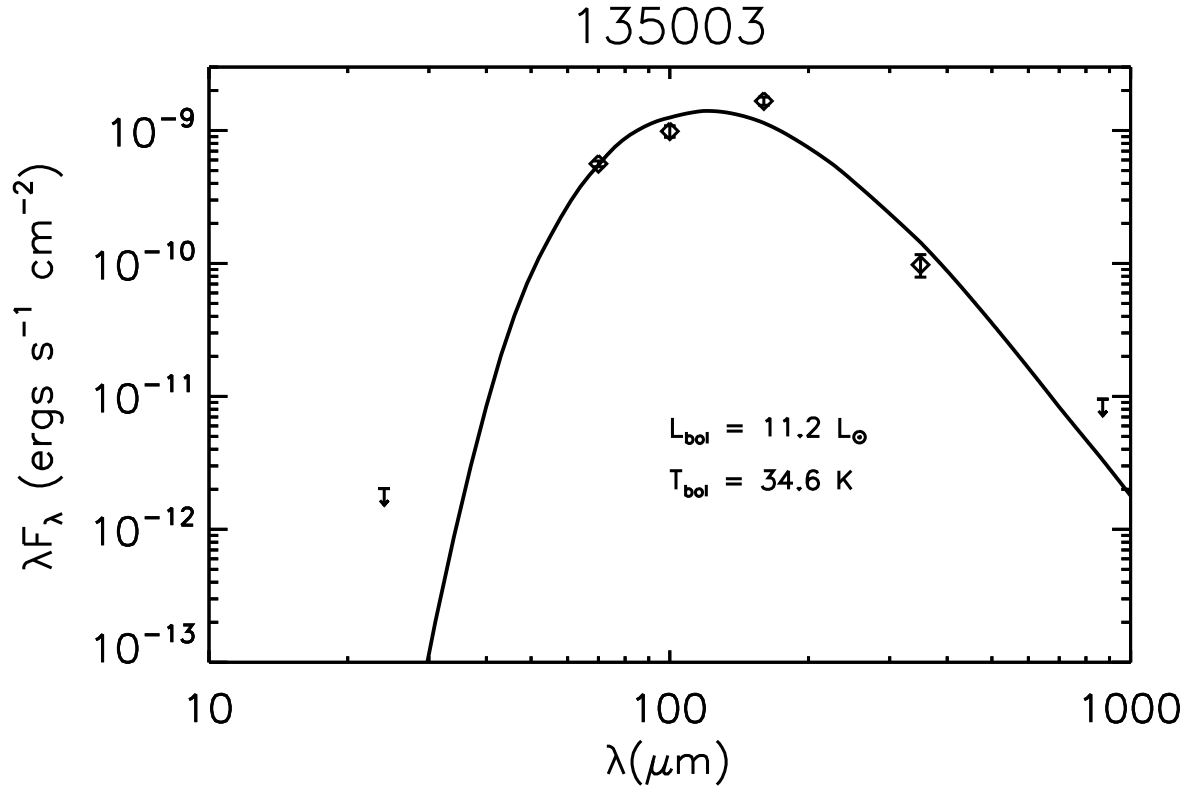


Fig. 8.— SED of 135003 including data from *Spitzer*, *Herschel*, and APEX. The APEX 870  $\mu\text{m}$  point is an upper limit due to source blending.

Table 1. CARMA 2.9 mm Observation Log

Source(s)	Date (UT)	Configuration	Calibrators (Gain, Flux)
093005, 091015	04 Oct 2012	D	0532+075, Uranus
090003, 082012 <sup>a</sup> , 302002	10 Oct 2012	D	0532+075, None
093005, HOPS373	12 Oct 2012	D	0532+075, Uranus
061012 <sup>b</sup> , 082005	13 Oct 2012	D	0532+075, Uranus
090003, 082012 <sup>a</sup> , 302002	15 Oct 2012	D	0532+075, Jupiter
061012 <sup>b</sup> , 082005	17 Oct 2012	D	0532+075, Uranus
119019, 097002	17 Jan 2014	D	0607-085, 3C84
119019, 097002	31 Jan 2014	D	0607-085, 3C84
135003, 019003	13 Feb 2014	D	0607-085, Uranus
135003, 019003	20 Feb 2014	D	0607-085, Uranus
093005, 090003, HOPS 373	09 Mar 2014	C	0607-085, Uranus
093005, 090003, HOPS 373	13 Mar 2014	C	0607-085, 3C84
082005, 097002, 082012 <sup>a</sup>	07 Mar 2014	C	0607-085, 3C84
082005, 097002, 082012 <sup>a</sup>	14 Mar 2014	C	0607-085, Uranus
091015, 091016	16 Mar 2014	C	0607-085, Uranus
091015, 091016	18 Mar 2014	C	0607-085, Uranus
091016 <sup>c</sup>	04 May 2014	D	0607-085, 3C84, 3C273

Note. — 0423-013 was used as the bandpass calibrator for all observations in 2012. The bandpass calibrator was 3C84 for all later observations.

<sup>a</sup>HOPS 372 is also in the field of 082012.

<sup>b</sup>HOPS 223 is also in the field of 061012.

<sup>c</sup>Data obtained through the CARMA FastTrack System.

Table 2. 2.9 mm Continuum Fluxes

Source	PBRs (yes/no)	HOPS ID	RA (J2000)	Dec (J2000)	$S_\nu$ (mJy)	Peak (mJy beam <sup>-1</sup> )	Noise (mJy beam <sup>-1</sup> )	Beam ( $''$ )	Mass ( $M_\odot$ )	$L_{bol}$ ( $L_\odot$ )	$T_{bol}$ (K)
097002	yes	404	05:48:07.71	+00:33:51.7	$45.7 \pm 2.5$	39.0	0.4	$3.31 \times 2.74$	$2.8 \pm 0.3$	1.14	33.4
HOPS 373	yes	373	05:46:30.99	-00:02:33.9	$51.1 \pm 4.2$	17.0	0.45	$2.08 \times 1.97$	$3.1 \pm 0.4$	5.2	36.0
302002	yes	407	05:46:28.28	+00:19:28.1	$47.1 \pm 2.5$	27.0	0.6	$5.00 \times 4.03$	$2.9 \pm 0.3$	0.85	28.6
093005	yes	403	05:46:27.90	-00:00:52.1	$90.0 \pm 4.8$	72.2	0.6	$2.42 \times 2.29$	$5.4 \pm 0.6$	1.7	30.8
091016 <sup>a</sup>	yes	402	05:46:10.01	-00:12:17.3	$46.6 \pm 2.7$	42.1	0.6	$2.15 \times 2.09$	$2.8 \pm 0.3$	0.65	29.1
091015 <sup>a</sup>	yes	401	05:46:07.72	-00:12:21.3	$30.9 \pm 2.6$	17.4	0.7	$2.19 \times 2.12$	$1.9 \pm 0.3$	0.81	30.9
061012	yes	397	05:42:49.03	-08:16:11.8	$17.0 \pm 3.1$	6.5	0.8	$5.58 \times 4.25$	$1.0 \pm 0.2$	0.75	32.1
HOPS 223	no	223	05:42:48.47	-08:16:34.3	$49.6 \pm 3.9$	28.2	1.0	$5.58 \times 4.25$	$3.0 \pm 0.4$	28.0	136.0
090003	yes	400	05:42:45.26	-01:16:13.9	$115.4 \pm 3.9$	83.3	0.55	$2.74 \times 2.56$	$7.0 \pm 0.7$	2.71	36.0
082005	yes	398	05:41:29.40	-02:21:16.5	$32.9 \pm 3.0$	21.3	0.4	$2.61 \times 2.4$	$2.0 \pm 0.3$	1.02	29.3
HOPS 372	yes	372	05:41:26.34	-02:18:21.6	$35.6 \pm 5.4$	10.2	0.7	$2.52 \times 2.38$	$2.2 \pm 0.4$	4.9	36.9
082012	yes	399	05:41:24.92	-02:18:07.0	$155.6 \pm 4.6$	87.5	0.6	$2.52 \times 2.38$	$9.4 \pm 1.0$	6.3	32.2
119019	yes	405	05:40:58.56	-08:05:35.0	$10.2 \pm 1.8$	4.0	0.5	$6.89 \times 3.71$	$0.6 \pm 0.1$	1.56	34.4
019003 A <sup>b</sup>	yes	394	05:35:24.23	-05:07:53.9	$38.9 \pm 0.9$	16.8	1.1	$5.58 \times 4.12$	$2.4 \pm 0.3$	3.16	33.6
019003 B <sup>b</sup>	no		05:35:24.86	-05:07:53.4	$52.7 \pm 0.9$	24.3	1.1	$5.58 \times 4.12$	$3.2 \pm 0.3$	< 0.5	<20.0
HOPS 68	no	68	05:35:24.27	-05:08:32.2	$41.8 \pm 5.9$	21.2	1.8	$6.91 \times 4.8$	$2.5 \pm 0.4$	5.7	92.9
HOPS 71 <sup>a</sup>	no	71	05:35:23.19	-05:07:45.1	$5.6 \pm 2.2$	9.4	1.1	$5.58 \times 4.12$	$0.3 \pm 0.1$	6.4	231.0
135003	yes	409	05:35:21.40	-05:13:17.5	$49.3 \pm 3.9$	16.9	1.0	$5.53 \times 4.14$	$3.0 \pm 0.4$	12.0	30.0
HOPS 59	no	59	05:35:20.15	-05:13:15.7	$40.4 \pm 6.5$	29.5	1.1	$5.53 \times 4.14$	$2.4 \pm 0.5$	49.5	479.0

Note. — Unless otherwise noted, the flux densities were measured in  $20'' \times 20''$  regions centered on the protostars and the positions were determined from Gaussian fits to the 2.9 mm data. The uncertainty of the integrated flux density is calculated from the uncertainty in the summation of all flux within the region;  $\sigma_{int} = N^{1/2} \sigma$ , where N is the number of independent beams within the integrated region and  $\sigma$  is the rms noise.

<sup>a</sup>Flux densities were measured in  $10'' \times 10''$  regions to avoid neighboring sources and negatives.

<sup>b</sup>Flux densities were derived from Gaussian fitting due to blended sources.

Table 3. Literature Flux Densities

Source	$S_\nu$ (mJy)	Distance (pc)	$L_{bol}$ ( $L_\odot$ )	$\lambda$ (mm)
L1448 IRS3B	$134.6 \pm 3.9$	230	5.0	2.7
L1448 IRS3C	$31.7 \pm 4.1$	230	1.0	2.7
NGC 1333 IRAS2A	$82.8 \pm 4.0$	230	20.0	2.7
NGC 1333 IRAS4A	$544.2 \pm 13.6$	230	5.8	2.7
NGC 1333 IRAS4B1	$180.3 \pm 7.9$	230	3.8	2.7
NGC 1333 IRAS4B2	$49.8 \pm 5.5$	230	3.8	2.7
L1551 IRS5	$173.3 \pm 7.5$	140	24.5	2.7
VLA 1623	$72.1 \pm 6.8$	125	1.0	2.7
IRAS 16293-2422	$1017.9 \pm 26.5$	125	15.0	2.7
Perseus 5	$4.0 \pm 1.0$	230	0.5	3.4
HH211	$43.4 \pm 2.0$	230	1.2	3.4
L1527	$32.6 \pm 6.0$	140	1.7	3.4
HH270VLA1	$6.3 \pm 1.0$	420	7.0	3.4
RNO43	$9.4 \pm 3.5$	420	12.5	3.4
IRAS 16253-2429	$1.8 \pm 1.0$	125	0.25	3.4
HH108MMS	$10.3 \pm 2.3$	300	0.7	3.4
HH108IRS	$35.7 \pm 4.9$	300	8.0	3.4
L1165	$12.1 \pm 1.7$	300	13.0	3.4
L1152	$15.2 \pm 2.8$	300	1.0	3.4
L1157-CARMA	$55.1 \pm 8.3$	300	5.0	3.4
RNO43	$26 \pm 6$	420	12.5	2.7
HH114MMS	$110 \pm 20$	420	26.0	2.7
IRAS03282+3035	$61 \pm 12$	230	1.2	2.7
IRAS04239+2436	$14 \pm 2$	140	1.1	2.7
IRAS20582+7724	$45 \pm 9$	200	4.0	2.7
IRAS21004+7811	$62 \pm 13$	200	1.0	2.7

Note. — The collection of 2.7 mm data at the top are from Looney et al. (2000), the 3.4 mm data are from Tobin et al. (2011), and the collection of 2.7 mm data at the bottom are from (Arce & Sargent 2006).

Table 4. 135003 Photometry

Wavelength ( $\mu\text{m}$ )	Flux Density (Jy)
24.0	$< 0.016$
70.0	$13.1 \pm 0.7$
100.0	$32.9 \pm 3.3$
160.0	$88.9 \pm 6.2$
350.0	$11.4 \pm 2.2$
870.0	$< 2.8$